2021

The Physics of Nanoaperture Optical Traps: Design, Fabrication and Experimentation

Chenyi Zhang
University of Central Florida

THE PHYSICS OFNANOAPERTURE OPTICAL TRAPPING: DESIGN, FABRICATION AND EXPERIMENTATION

by

CHENYI ZHANG
B.S. Shanghai University, 2016

A dissertation submitted in partial fulfillment of the requirements
for the degree of Doctor of Philosophy
in CREOL
in the College of Optics and Photonics
at the University of Central Florida
Orlando, Florida

Spring Term
2021

Major Professor: Ryan. M. Gelfand

ABSTRACT

Recent progress in nano optics, spurred by progress in nanofabrication, has allowed us to overcome these challenges. We use surface plasmon polaritons to break the optical diffraction limit and squeeze the photon energy into a local hot spot. The small mode volume of a plasmonic antenna or nanoaperature significantly enhances the local field and can be designed to resonate at a desired wavelength. By designing, fabricating, and testing these nanoapertures, I trap single nanoparticles with significantly reduced laser power by measuring the monochromatic transmission change of a resonant aperture. A freely diffused nanoparticle, behaving like a dipole antenna, interacts with the nanoaperture when trapped and shifts the resonance of the nanoaperture. By only monitoring a single wavelength, the presence of the particle changes the transmission signal. The effect of particle-induced transmission spectrum shift is called the self-induced back-action effect. This particle-induced spectrum change increases the transmission amplitude and variance once trapped. Furthermore, the monochromatic transmission measurement is a faster detection method than the spectrum measurement. It is able to follow up the diffusion, folding or conformation change of the trapped particle.

Key word: *nanoaperture, trapping, single molecule, plasmonic effect, nanofabrication, focused ion beam*

ACKNOWLEDGMENTS

I would like to send my deepest thanks to my mother and father for their love and encouragement. They are the best parents in the world. Their full support for my studying abroad gives me power to start the journey.

My sincere appreciation also goes to my advisor, Dr. Ryan. M. Gelfand. He gives me the opportunity to study, understand and explore optics. The four-year mentorship leaves me good memory and lessons in both research and life.

The special thanks also go to my committee, Dr. Kyu Young Han, Dr. Ellen Hyeran Kang and Dr. Stephen M. Kuebler, for their help and precious suggestions during the research. Especially, I cherish the time with Dr. Han discussing about the optical, proteins and biology topics. My collaborator in Oak Ridge National Labs, Alex Belianinov, not only for his help on my research but also the satisfying discussion on culture and values.

I also would like to thank my partner, Xiaowen, who has been always by my side and support me. I also appreciate the generous help all my labmates, Ben, Jinhan, Vahid, Crystal, Jialei, Zheyuan and Ruitao, in study and life. The acquaintance with you are the most beautiful part in my graduation study.

Finally, I would like to thank the publishers for the reprints of the published papers.

TABLE OF CONTENTS

LIST OF FIGURES

LIST OF TABLES

LIST OF ACRONYMS (OR) ABBREVIATIONS

AuNP – Gold nanoparticles

DOS - Density of states

DLS – Dynamics light scattering

EDL – Electric double layer

FRAP – fluorescence recovery after photobleaching

FRET – fluorescence resonance energy transfer

LSP – Localized surface plasmon

NAOT – Nanoaperture optical trap

OT – Optical tweezer

QD – Quantum dot

SD – Standard deviation

SIBA – Self-induced back-action effect

SPR – Surface plasmon resonance

CHAPTER ONE:
INTRODUCTION

The extensive development of nanotechnology involves high-resolution detection and calibration tool in nanomedicine[1], film morphology[2], neuron imaging[3], nanophotonic circuit[4], etc. Recent research has shown an abundance of proof that nanoparticles behave differently than bulk material. The surface-volume ratio of the nanomaterial is significantly larger than the bulk material, resulting in quantum confinement[5], unpaired spins[6] and uncompensated bonds[7]. The study of the molecules in nanosize attracts various attention in particle size distribution, diffusion dynamics, structure-function relationship, charge or energy transfer. These revolutionary results have led to great developments in nanotechnology.

A lot of characterization methods have been developed to quantize the nanoparticle property. The light scattering techniques (dynamic light scattering (DLS)[8], fluorescence recovery after photobleaching (FRAP), X-ray diffraction and FT-IR spectroscopy) and FT-NMR are the ensemble measurement to characterize the molecules or crystals in the gas, liquid, and solid phases. Whereas some intrinsic properties of the single molecules (photobleaching, size or shape inhomogeneity) are hard to be identified. Optical diffraction also set a limitation to the spatial resolution. The optical beam is not able to resolve the nanosized particle when they are close to each other. Due to the optical diffraction limit, the DLS and FRAP are ensemble measurements, determined by statistical analysis. The measurement averages out the characteristics and function-dependent heterogeneity of a single molecule[9]. The information from the heterogeneity might reveal the additional chemical or physical properties in diffusion, adsorption-desorption dynamics, folding–unfolding dynamics, trapping, or other processes. The broadening of the spectrum of x-

ray diffraction from the size distribution and conformational heterogeneity is hard to quantify. The single-molecule experiments naturally offer the opportunity to these random processes (stochastic process). It can provide direct observation of the kinetic coefficient of a sequential dynamic process[10, 11]. Those complex assembly processes and polymerization can be out of phase and cancel each other in ensemble measurement losing the details of the individual steps. Furthermore, molecule properties are reflected by interacting with its environment and complexes. Single-molecule method measures the short-lived or transient states that require higher temporal resolution by measurement of the binding strength, charge and mass[12].

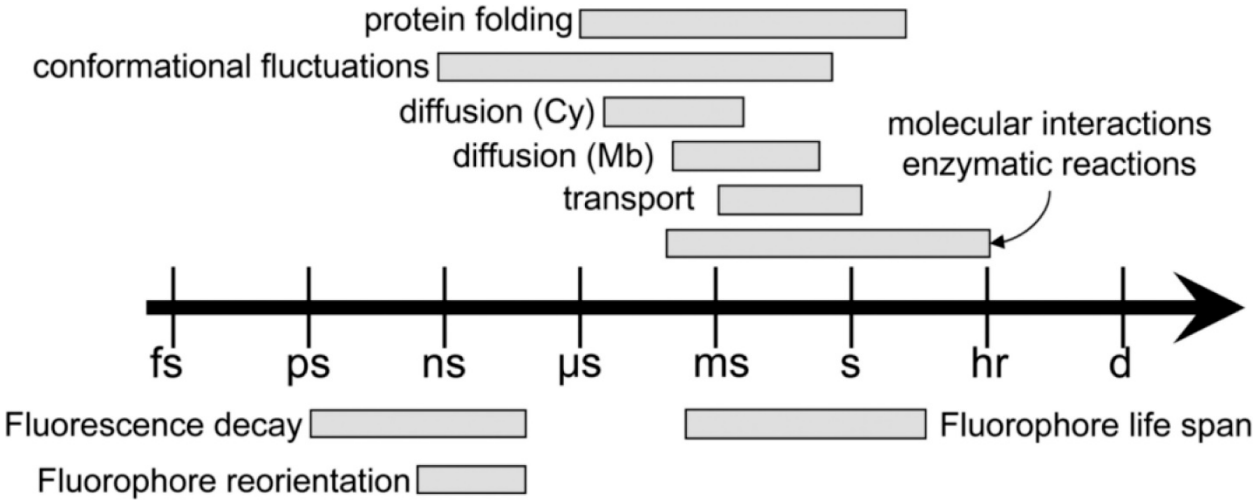

Figure 1: Time scale of single-molecule studies in biology. Reprint from ref[11]

The single-particle tracking records the trajectory of the diffusion motion of a single nanoparticle with an optical microscope. The explains the catalysis and the solvent effect on the cell membrane and proteins[13]. The identification methods range from mass, polarizability, charge, etc. Interferometric scattering (iSCAT) uses the interference of the scatted beam from the sample and reference beam to track the particle motion in time[14]. The method discovers the myosin motion along the actin at nanometer precision and millisecond frame rate. Also, the recent

breakthrough has shown the mass measurement down to 3kDa with this technique[15]. Due to the scanning speed of the detector, this method is limited by the temporal resolution. AFM investigates single molecules employing force detection. The setup can be simplified as a tip-shaped (1~20nm) cantilever linked to a piezo actuator and a grounded planar substrate. Yang Zhao et al. probe the sub-piconewton chiral forces with an AFM tip of chiral structure, which boosts the resolution of chiral detection to 2 nm resolution[16]. However, the large stiffness of the AFM limits its application on conformation analysis, which is a promising field in drug development and functional characterization.

Table 1: Recent emerging single molecule methods

Single Molecule Method	Temporal Resolution	Observation Time	Concentration limitation	Label Free	Tether Free	Measurement
atomic force microscopy	>20ms	minutes	20 μM	Yes	No	Force
interference scattering (iSCAT)	50 μs	minutes	0.1 nM	Yes	Yes	Scattering intensity
Immobilization FRET (TIRF)	10 ms	1 – 3 minutes	10 nM	No	No	Fluorescence
Single Molecule FRET	1 – 10 μs	1 ms	1 – 2 nM	No	Yes	Fluorescence
Zero Mode Waveguide	10 ms	> 1 minute	1 μM	No	No	Fluorescence
ABEL Trap	1 – 10 μs	> 10 s	1 – 2 nM	No	Yes	Fluorescence
Nanoaperture Optical Trap	1 ns	> 1 minutes	No Limit	Yes	Yes	Transmission

To enrich the spectrum of measurement and compensate for the speed limitation and spatial resolution, the nanoaperture trap (NAOT) is now under study. Conventionally, Optical trapping uses focused laser beams has been applied in the manipulation of the micro-objects, atom cooling, microfluidics and micromotors[17]. However, there are three main challenges in the optical trapping technique. First, the trapping potential is inversely proportional to the fourth-order of the volume of the objects. The photon-induced beam power (intensity) can burn and destroy the micrometer or nanometer biomolecules in biology applications [18]. Thus, the mainstream of

single-molecule trapping techniques is prone to use non-destructive small power laser (~1mW) to manipulate the biomolecules. Second, the optical tweezer is restricted by the diffraction limit. The beam waist can contain a few nanoparticles but cannot guarantee the number of the trapped objects[19]. Thirdly, to control the particle number in the trap, the immobilization strategy[20], such as tethering and labeling, is applied to the particle of interest. The binding of one site of the protein changes the conformation or denature of the protein, which affects the sensitivity of other sites. This well-known phenomenon is called allosteric interaction[21-23]. The label-free trapping technique[24] levitates the interactions of the atomic local field of the protein with subtle trapping forces and thus overcoming the allosteric effect induced by unnecessary bindings. To cope with these problems, nanoaperture optical trap (NAOT) uses plasmonic effect to break the diffraction limit and do not need to tail the beads to the particles of interests. This method is able to avoid steric hindrance.

This thesis is going to discuss the nanoaperture optical trap (NAOT) from design to measurement. It is arranged into six chapters: chapter one discusses the motivation and the history of the NAOT method; chapter two discusses the theory and the working principle of the NAOT; in chapter three, the simulation results give a numerical prediction of the nanoaperture property and the spectrum behaviors during the trapping; Chapter four focuses on the fabrication and nanoaperture calibration; in chapter five, I conclude all the sub-10nm trapping experiment with the NAOT and prove the trapping ability of this NAOT method. Chapter six is a summary of the work and leaves some hints for future work.

CHAPTER TWO:
BACKGROUND

Gradient force in optical tweezers

The optical tweezer (OT), since its invention, has drawn a lot of attention to its ability in manipulating particles in air, vacuum and liquid[25]. The Nobel prize awardee, Arthur Ashkin demonstrated the first experiment to optically manipulate a micro-sized particle in water[26]. A variety of techniques have been developed to expand the application of the OT for bacteria[27], living organisms, chromosomes[28] and red blood cells *in vivo*[29]. Circularly polarized beams provide angular momentum to the particles to study viscoelastic properties of bio-fluids or create micromotors[30]. In a vacuum and at absolute zero temperature, the laser beam is used to cool the atom to negative absolute temperature and excite superfluid helium[31].

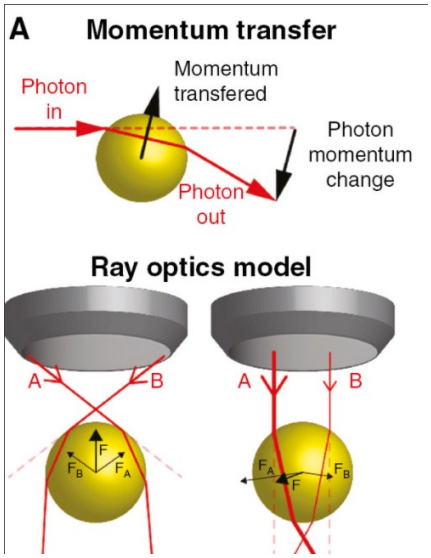

Figure 2:sketch of the gradient force in optical tweezer. Reprint from ref [25].

The OT is created by a tightly focused Gaussian beam, thereby forming a gradient force at the diffraction-limited focal point and radiation pressure force along the optical axis. Scattering

force is also created but it is negligible when trapping the small particles. When the trapped particle has a refractive index larger than the medium, the gradient force is pointing toward the focal point. On the contrary, the one with a smaller refractive index than the medium is pushed away from the intensity focal. The momentum is transferred from photons to the particle refracting the light.

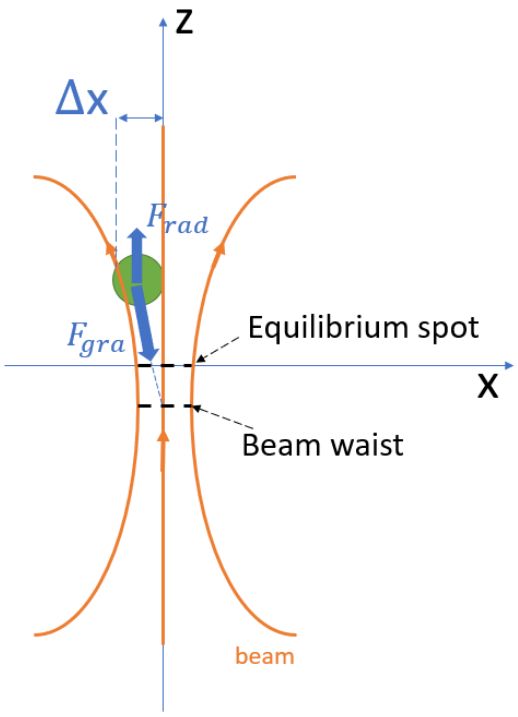

Figure 3: a sketch of the optical trapping where the gradient force is pointing to the beam waist (focus). The particle is able to be trapped within the vicinity of the equilibrium spot

When the gradient force overcomes the radiation pressure force and the Brownian motion of the particle, the particle is trapped, oscillating about the equilibrium point but not the focal point. The optical forces, about tens of piconewtons, are significant on microparticles, even can slow down the blood flow[29]. The magnitude of the gradient force and its potential are

$$F_{gra} = \frac{1}{2}\alpha\nabla E^2 = \frac{2\pi n_0 a^3}{c}\left(\frac{m^2-1}{m^2+2}\right)\nabla I(r) \qquad (1)$$

$$U = \frac{1}{2} n_m Re[\alpha(\omega)] E^2 \quad (2)$$

where α is the polarizability of the particle. According to the Mie theory, the polarizability is proportional to the volume of the particles. m is the ratio of the refractive index of the particle and medium. In Ashkin's work, a stable trap needs a potential depth larger than $10k_BT$ to overcome the Brownian motion[32].

However, It is very challenging to trap the nano-size particle under 100nm with the optical gradient force. The decrease of volume diminishes the gradient force while Brownian motion is dominant. Increasing the beam power will deform the macromolecules with photon-induced thermal effect[33].

Nanoaperture optical traps (NAOT)

The free space OT is an innovative tool to study single particles. However, when the size of the trapping objects reduced to 100nm, the optical beam by nature has a diffraction limit where a few particles gather at the focal points break the single-molecule condition and change the local concentration significantly. Thus, the research has been migrated from the free space to nano resonators. Nanoaperture optical trap (NAOT), utilizing a metallic nanoaperture to break the diffraction limit and trap a single particle. In this section, we are going to discuss the major theories behind the NAOT.

Polarizability

Polarizability is a parameter describing how the external electric field changes the distribution of the electrons in the media. It provides one of several parameters in the description of molecular structures[34] and conformations[35]. In atoms with larger electron numbers are hard

to control the valence electrons in the outer orbit. When a dipole is posed in an external electric field, the electrons of the dipole have more tendency to move along the electric field (more polarizable) and vice versa. Based on the molecule polarizability, slowing, cooling and trapping neutral particles in the static field or high-frequency electromagnetic field is exploit[36].

Different from the refractive index of bulk, polarizability (α) is a molecular property related to molecule orientation and bond length (dipole momentum p) under the external field E.

$$p = \alpha \cdot E \quad (3)$$

For isotropic media (such as a gold sphere), polarizability can be simplified to scalar from polarizability tensor. The x-polarized external electric field only polarizes the atoms of the media along the x-direction but does not affect the atoms in other directions (y or z). Under this condition, the polarizability of a sphere can be related to the dielectric constant according to Clausius-Mossotti relation:

$$\frac{4\pi}{3} N_a \alpha = \frac{M}{p} \left(\frac{\varepsilon_r - 1}{\varepsilon_r + 2}\right) \quad (4)$$

N_a is Avogadro constant. M is molar weight. ε_r is relative dielectric constant. The permanent polarizability of a sphere isotropic beads can be calculated in the following equation:

$$\alpha = 4\pi r_c^3 \left(\frac{\varepsilon_r - 1}{\varepsilon_r + 2}\right) \quad (5)$$

Light-matter interaction: metal, Drude model and plasmonics

Metals are widely used in our daily life. They have free electrons in a lattice of positive ions. The electrons oscillate with the external field and collide with each other with a damping rate $1/\tau$. The oscillating electrons form an effective dipole and generate polarization P. For most metal,

the damping rate fall in the range of hundreds of terahertz and close to plasma frequency. The real part of the permittivity is close to 0 and the penetration of the visible band is low. In low frequency, bulk metals are a good conductor of electricity, where the imaginary part of permittivity is 0. Free electrons transfer electricity along its surface. They are also used as mirrors due to the high reflectivity in the mid-infrared band and limited penetration depth through it. However, when the frequency reaches to the visible and near-infrared band, the penetration depth is increased depending on the wavelength and so does the dissipation. The amount of energy dissipation can be described with the complex dielectric function $\varepsilon = \varepsilon_1 + i\varepsilon_2$ which shows the phase change with respect to the external driving field.

$$\varepsilon_1 = n^2 - \kappa^2 \quad (6)$$

$$\varepsilon_2 = 2n\kappa \quad (7)$$

κ is the extinction coefficient, determining the absorption of EM waves propagating through the medium. With Beer's law, the absorption coefficient and extinction coefficient illustrate the exponential attenuation of the intensity of a beam propagation:

$$\alpha(\omega) = \frac{2\kappa(\omega)\omega}{c} \quad (8)$$

Thus, the imaginary part of the dielectric function ε_2 determines the absorption of the medium. Electromagnetic fields are transverse waves. Deriving from the dispersion relation, a longitudinal collective oscillation can only occur at:

$$\varepsilon(\omega) = 0 \quad (9)$$

Metal, in the plasma model, can be explained as the free electron gas moves against a fixed background of positive ion cores. However, this model does not take lattice potential and electron-electron interaction into consideration. The assumption is made that the electron with optical effective mass exists in a band structure. The electron follows the oscillation of the external EM field with a damped motion of collision frequency (damping rate) $\gamma = 1/\tau$. At room temperature, this damping rate γ is about 100THz. The real and imaginary part of the dielectric function of the metal with the ideal free electron is

$$\varepsilon_1(\omega) = 1 - \frac{\omega_p^2 \tau^2}{1+\omega^2\tau^2} \quad (10)$$

$$\varepsilon_2(\omega) = \frac{\omega_p^2 \tau^2}{\omega(1+\omega^2\tau^2)} \quad (11)$$

$$\omega_p^2 = \frac{ne^2}{\varepsilon_0 m} \quad (12)$$

This is also known as the Drude model. ω_p represents the plasma frequency and usually are 5~15eV in the ultraviolet regime. At plasma frequency, all the electrons move in phase and the wavevector is infinite. In the realm of gold film, when $\omega > \omega_p$ and s free electrons dominant the optical response, the interband (d band) close to the Fermi surface leads to a highly polarized environment. Thus, the Drude model need a correction as

$$\varepsilon(\omega) = \varepsilon_\infty - \frac{\omega_p^2}{\omega^2+i\gamma\omega} \quad (13)$$

It is also, later on, experimentally determined by Johnson and Christy in 1972. Gold and silver can break down at the boundary at NIR and VIS band. For these noble metals, photons

efficiently excite interband transitions while the electrons are pumped from the band lower than the Fermi surface to higher bands.

As shown in Figure 1, the simplest geometry of SPP is the single, flat interface of a dielectric media with positive real ε_2 and a conductor media with dielectric function ε_1. X axis is the propagation direction and the propagation wavevector β is a complex number. At the condition of frequencies below the bulk plasmon frequency ω_p, the conductor media dielectric function $\varepsilon_1$is required to fulfill the dispersion relation:

$$\beta = k_0\sqrt{\frac{\varepsilon_1\varepsilon_2}{\varepsilon_1+\varepsilon_2}} \quad (14)$$

$$k_{zi} = \sqrt{\beta - \varepsilon_2(\frac{\omega}{c})^2} \quad (15)$$

k_0 is the wavevector of the incident wave in a vacuum. From the equation, we find the real part of the dielectric function should be negative and large if the damping is neglectable. k_{zi} is imaginary. Thus, surface plasmon polaritons are electromagnetic excitations propagating at the dielectric-conductor interface. No SPP exists with TE mode. The TM wave around the interface excites the collective excitation of surface plasmonic polaritons along the metal-dielectric boundary. The evanescent field extends perpendicular to the interface. The imaginary k_{zi} leads to micron-scale field confinement in both dielectric and conductor sides. The plasmon propagation length L is inversely proportional to the magnitude of β. If the conductor has larger damping, the distinction coefficient and magnitude of the propagation wavevector are larger. As expected, the propagation length is accordingly smaller.

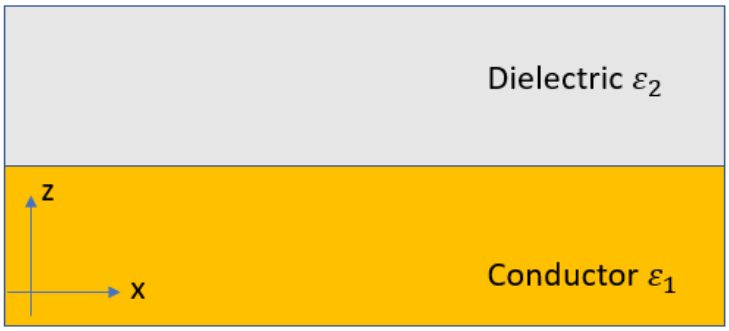

Figure 4: 2D layered geometry for SPP material

To keep the propagation wavevector real, the magnitude of the SPR propagation wavevector should be smaller than the wavevector of the incident beam along the x-direction $k_{x,d} = \sqrt{\varepsilon_2} k_0 \sin(\theta)$. To excite the SPR, many methods are used to match the phase condition, such as gratings, prisms, and focused beams.

Local surface plasmonic resonance and plasmonic cavity

For the metallic nanoparticles (NP) with a size comparable to the metal skin depth, the electric field of the incidence light can penetrate the metal and polarize the conduction electrons. Compared with SPP, plasmons in NPs, much smaller than the optical wavelength, do not propagate along the surface, called localized surface plasmons resonance (LSPR). The surface-volume ratio of the NP is much larger than the counterpart in bulk. The electron-free mean path is much shorter. Thus, the damping in the NP is different from the one in bulk.

$$\gamma = \gamma_{bulk} + A\frac{v_F}{d} \qquad (16)$$

Here, d is the mean free path and v_F is Fermi-velocity. The former illustrates the collision-free distance of an electron. Fermi velocity is corresponding to the Fermi energy level of the electrons. For the simplest case, the particle is a sphere. The multi-scattering and absorption process inside the NP triggers plasmons oscillation in the NP relating to the particle sizes.

$$Q_{abs} = 12\ \frac{2\pi\sqrt{\varepsilon_2}a}{\lambda_0}\ \frac{\varepsilon_2\, Im[\varepsilon_1]}{(Re[\varepsilon_1]+2\varepsilon_2)^2+Im[\varepsilon_1]^2} \quad (17)$$

$$Q_{sca} = \frac{8}{3}\ \frac{2\pi\sqrt{\varepsilon_2}a}{\lambda_0}^4\ \left(\frac{\varepsilon_1-\varepsilon_2}{\varepsilon_1+2\varepsilon_2}\right)^2 \quad (18)$$

a is the radius of the particle. Both scattering and absorption are related to the volume of the particle. The scattering dominants in relatively larger particles while absorption is turned on for smaller particles. And maximum absorption happens at the frequency where $Re[\varepsilon_1] + 2\varepsilon_2 = 0$. This is the LSPR condition. Meanwhile, a phase delay, determined by the imaginary part of the metal permittivity, leaves are large damping and loss in LSPR. The line width of the resonance is wider than SPR. The quality factor of the LSPR is around 10~30.

As for the particles of small sizes (less than 50nm), the LSPR can be simply modeled as a harmonic oscillator with effective mass parallel to the incident excitation. The incident beam needs to align with the oscillation frequency to excite the LSPR. The displacement of the electrons from the lattice generates a restoring field to pull back the polarized electrons as shown in Figure 2. The total field of an electromagnetic field is a sum of the external field and the restoring field from the particles. When the two LSP systems are posed close enough to each other, the coupling of the restoring field of the particles has an impact on the total field.

The two particles sit along the polarization direction. Due to the confinement of the plasmon electrons, the LSPs oscillate with the external field. The inter-particle field is in the

opposite direction to the external field[37]. Despite the damping, this inter-particle field increases when the distance of the particles is decreased. When the alignment of the two particles is perpendicular to the polarization of the external field, the interparticle field is in the same direction as the external. The stronger coupling of the field leads to stronger energy of the near field and a blue-shift of the spectrum.

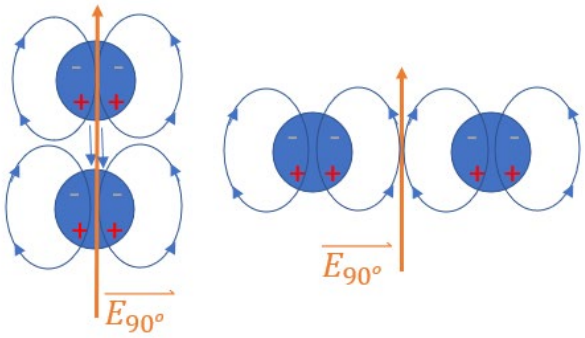

Figure 5: Sketch of two closely spaced nanoparticles under an excitation field, (left) a pair of close particles with the polarization of the exciting field parallel to the long particle pair axis and (right) perpendicular to the long particle pair axis.

A nanoaperture in a flat metallic surface can also confine an LSP while the whole is an inverse structure of a nanoparticle. the plasmonic nanoaperture acts as a dipole nanoantenna since its size is much smaller than the wavelength, acting like a dipole emitter[38]. The plasmonic effect confines the photon energy to a local collective free electron at the metal-dielectric interface. Due to the large losses (damping and heat), the plasmonic cavity features a small effective volume of the cavity and an abundant local field enhancement (20~100 times) and is called 'hot spot'. The tiny spatial confinement and the damping also leads to a fast decay rate on the order of femtosecond. The LSP resonance can be tuned by changing the geometry of the nanoaperture. We will discuss the aperture design later in Chapter 2.

The excitation condition of LSP is much easier than SSP. The fabrication requirement is lower since SSP needs a monolayer structure. The LSP is dependent on the size of the particle where the spectrum is easier to be tuned based on appropriate design.

Self-induced back-action effect

Plasmonic traps uses resonant metallic pillars, breaks the diffraction limit and improves the spatial resolution down to angstrom. However, the near field enhancement creates the same gradient forces for trapping. Those isolated metallic pillars still do not solve the heat problem. This section introduces a concept of 'self-induced back-action effect (SIBA)' raised by Dr. Quidant and Dr. Gordon to relax the requirement in intensity[39, 40].

The key physics in SIBA is the interaction between the metallic nanocavity and the nanoparticle (based on the particle position)[41]. The particle size much smaller than the optical wavelength can be regarded as a dipole (dipole approximation). The dipole induces a dipole moment under the effect of the EM field as mentioned in the Polarizability section. Within the range of plasmonic field, the particle couples with the nanocavity and alters the resonance frequency of the cavity. namely, the motion dynamics of the particle affect the intensity spectrum and also the trapping force. The particle can be trapped in a dynamical intensity minimum and reduce the effect of photo-thermal damage. The back-action parameter $\eta = \frac{\alpha(\omega)}{\varepsilon_0 V_m} Q \propto \frac{V_{particle}}{V_{cavity}}$ characterizes the system performance, where Q is the resonator quality factor, ratio of the central frequency and linewidth:

$$Q = \frac{\omega_c}{\kappa} \quad (19)$$

This quality factor reflects the decay time of the cavity κ^{-1}. The photonic cavity of high Q is around 10^6 and its decay time is on the order of nanoseconds. The plasmonic cavity of the modest Q is below 100 and the decay time is up to terahertz. Both decay times are significantly shorter than the Brownian motion of the particles. The cavity can respond to the particle motion instantaneously. The plasmonic in this case is more superior to the photonic cavity. This feature makes it possible to break the time-resolution limitation for detecting protein-small molecule interaction with SIBA trapping.

Since the particle is much smaller than the incidence wavelength, the electric field is assumed as a constant for a single trapped particle. Thus, the particle is a point source with polarizability $\alpha(\omega)$. It is natural to relate charge distribution and intensity and frequency of the incidence to polarizability. Despite the internal and external coupling, the aperture-particle system is featured with particle-position-induced fluctuation. When the particle is trapped in the nanocavity, the coupling in between is due to the superposition of quantum states and leads to a resonance shift $\triangle$ from ω_c to ω. The charge distribution fluctuation of the particle has a much smaller frequency shift compared to the resonance frequency of the empty cavity. In experiments, the optical force is related to the intensity and the cavity and particle polarizability. Within the lowest order of the perturbation theory, we can compare the frequency shift of the cavity when the particle is present in the cavity:

$$\delta\omega(x) = \omega_c \frac{\alpha}{V_m \varepsilon_0} f(x) \qquad (20)$$

where ω_c is the resonance frequency of the empty cavity, V_m is mode volume in the cavity, α is polarizability of the particle of interest. It is worth noting that the particle polarizability is

proportional to the volume and the shape of the particle. $f(x)$ is a normalized intensity linewidth of the empty cavity. Thus, the frequency shift $\delta\omega(x)$ is on the order of central frequency and not negligible. All the parameters except the polarizability of the particle are positive. For most materials with positive polarizability, the spectrum is always redshifted. Herein, from the Hamiltonian equation and Heisenberg-Langevin equations, the transmission of the cavity-particle system can be derived as an equation of photon number of the particle-cavity system:

$$n(x) = 4E_0^2 \frac{\kappa_{ex}}{\kappa} \frac{1}{1+(\eta f(x)+\triangle)^2} \quad (21)$$

where κ_{ex} refers to the decay rate of the external coupling of the cavity; $\eta \propto \frac{\alpha(\omega)}{Vm} Q$ is defined as a back-action parameter, proportional to the polarizability of the trapping particle, Q factor of the cavity and the inverse of the cavity mode volume; $\triangle = \frac{2(\omega_l - \omega_c)}{\kappa}$ is a detuning factor, the difference between the excitation frequency ω_l and cavity resonance ω_c; $f(x)$ is the normalized beam profile. To get the maximum photon number out of the system, $\eta f(x) + \triangle = 0$ is the resonance condition. The position x is the resonance position. When the particle locates at $f(x) \ll 1$, the coupling effect is weak and no spectrum shift occurs.

When it comes to the dynamics of a trapped particle in the cavity, the time-averaged potential for an empty DNH system is

$$U(x) = -2\hbar E_0^2 \frac{\kappa_{ex}}{\kappa} arctan\,[\eta f(x) + \triangle] \quad (22)$$

According to the potential function above, two extreme conditions can be discussed on the back-action parameter: Upon a small enough back-action parameter ($\eta \ll 1$), the potential is reduced to $\mathrm{U(x)} = -\mathrm{Re}(\alpha)|\mathrm{E(x)}|^2$. The system does not have a spectrum shift. Therefore, to trap

a dipole without a cavity, the system requires a larger incidence intensity. On the other hand, a high η results in saturation of arctan() by $\pm\frac{\pi}{2}$, which means the trapped particle is confined in an area with two high potential walls.

When a laser beam at frequency ω launches into a cavity, the intracavity response is in the shape of a Lorentz curve. Then, in Taylor expansion the response refers to frequency is:

$$I(\omega) = I_0 \frac{(\Gamma/2)^2}{(\omega-\omega_c-\delta\omega)^2+(\Gamma/2)^2} \approx I_{cav} - \frac{2\delta\omega(\omega-\omega_c)}{(\omega-\omega_c)^2+\left(\frac{\Gamma}{2}\right)^2} I_{cav} + \cdots \quad (23)$$

where $I_{cav} = I_0 \frac{(\Gamma/2)^2}{(\omega-\omega_c)^2+(\Gamma/2)^2}$ is the intensity of the empty cavity. The Talyor expansion above shows the contribution of the empty cavity and the trapped particle. The second item shows the intensity fluctuation due to the position and polarizability of the particle[39]. The motion of cavity-particle system is assumed to follow overdamped Langevin equation:

$$\gamma\dot{x}(t) + \kappa_{tot}x(t) = \xi(t) \quad (24)$$

where γ is viscosity, κ_{tot} refers to the stiffness of the trap (responsivity of the system) and $\xi(t)$ is thermal fluctuation due to Brownian motion. There is no requirement on the particle resonance but polarizability.

<u>0D semiconductor: quantum dots</u>

In semiconductor, the optical absorption is due to the photon-induced transitions from occupied electron states to available unoccupied states. The electron transition energy needed is the band gap. The occupied states are in conduction band while the unoccupied is valence band. Semiconductor has continuous band while metal is a two-state system. The term density of states

(DOS) is a term to illustrate the number of available states in the continuous energy band. Bohr radius, originally, is defined as the distance between the nucleus and the electron in a ground-state hydrogen atom model[42]. When a particle has a small enough size comparable to Bohr radius(kr ~0), the energy band is not continuous anymore. Instead, the quantum effect is dominant. The particle has discrete energy states.

Quantum dots (QD) are called artificial atoms for the tiny sizes. The size property of the quantum dots makes them superior in biological imaging[43], catalysis[44], optoelectronic devices, lasing[45, 46], and solar energy conversion[47-49]. They are considered as a dipole without dimension (dipole approximation). Thus, QDs are analyzed as particle in the box model. Photon illumination on a QD generates exciton(s). The exciton is an electron-hole pair in a bound state excited out of the valence band. The pair is bounded with Coulomb interaction like the hytrogen model mentioned before. The exciton Bohr radius is the distance of the exciton pair and depends on the material types. In this bound state the electron still has characteristics similar to that of free electrons, but its energy is a little lower than that of conduction band electrons. The binding energy of the exciton ranges from a few millielectronvolts to a hundred millielectronvolts, leading to absorption below the material bandgap. Due to the coulombic interaction, the linear optical response of the QD (under weak field) is govenerned by the size of the QD. When the radius of the particle is on the same order as the exciton Bohr radius (CdSe ~5.8nm), the QD behaves like a semiconductor with discrete quantized energy states. Those nanocrystals experience the quantum confinement of the exciton.

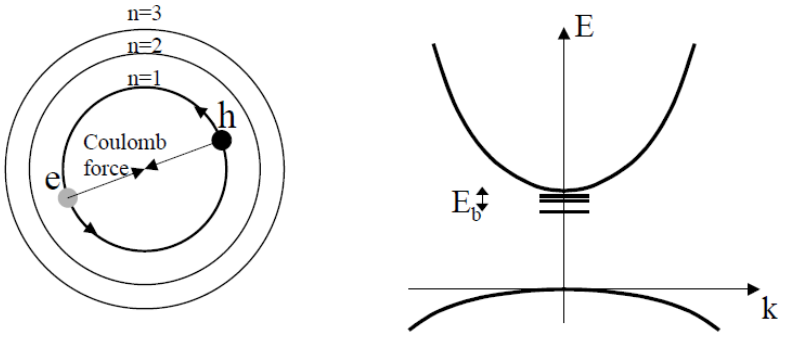

Figure 6: Sketch of the exciton generation (left) and band structure of the corresponding exciton states (right)

The sum of the energy of an exciton is consisted of band gap energy, confinement energy and bound exciton energy. The confinement energy is dependent on the particle size[45]. The larger dots have a larger emission wavelength and vice versa. The bound exciton energy is inversely proportional to the second order of the dielectric constant and proportional to Rydberg's energy. The latter is negligible unless the size of the particle is smaller than the Bohr radius.

After photon absorption larger than bandgap, the electron and hole are generated but not stationary. the non-radiative electron needs a period of time to relax to the lowest level of the valance band (non-radiative decay time. Then spontaneous emission is from the recombination of the exciton and competes with the non-radiative process [7]. The rate of non-radiative (dim) state of the quantum dots is attributed to the Auger recombination and slow decay time (ns). Decline in the decay time of the non-radiative state results in higher photoluminescence efficiency. The external field introduces charge separation and exciton dissociation, which can quench the nanoparticle. The details will be discussed in the quenching section later. The electric field and quantum confinement Stark effect (non-radiative states broaden the discrete absorption and emission band) exhibits dipolar character both in the ground excited states[50]. The dipole moment is enhanced when the quantum dots is in a transition to the first exciton state[51]. The research in

blinking of the quantum dots shows that multiple excitons and the damping rate results in quantum efficiency and particle charging. This excited state also encompasses different multiexciton states of different polarizability, such as a trion (triplet exciton)[52], a biexciton and a triexciton. Compared to typical molecular, these excited state of the QD possess a polarizability as high as 10^5 A^3, which is 3 to 4 order larger than some typical molecules[53].

To stabilize the quantum dots, shell-core structure (i.e. CdSe/CdS colloidal quantum dots) are designed. The shell is able to passivate the core and isolate it from the surrounding microenvironment, increase the potential energy barrier for exciton confinement within the core, and provide the protection against degradation or oxidation.

Purcell effect

The rate of the spontaneous emission of an emitter is attributed to the probability of transition in the optical states. This probability is concluded in Fermi's golden rule, which is not only rely on the intrinsic properties of the emitter but also involves the photonic environment. The density of optical states (DOS) quantifies the number of the available states of the emitter in a homogeneous medium and decides frequency of the light to be emitted. Introducing inhomogeneity changes the photonic environment and leads to an altered local density of optical states (LDOS). Specifically, by creating a resonant environment for a certain frequency, the LDOS at that frequency dramatically increases.

The interaction of a dipole and the light can be modified by changing the surrounding dielectric environment. When a system coupled to an electromagnetic resonator, the spontaneous emission probability exceeds the bulk material alone and the recombination time (decay time) is

reduced. An emitter experiences the increased LDOS and emits photons more efficiently; its excited state lifetime decreases on resonance with a cavity mode. In an off-resonant cavity, it is also possible to reduce the LDOS at a certain frequency, suppressing emission. This phenomenon was included in E. M. Purcell's paper in 1946. The quantity of the spontaneous emission rate enhancement is defined as Purcell factor[54]:

$$F_p = \frac{3}{4\pi^2}\left(\frac{\lambda_c}{n}\right)^3 \frac{Q}{V_{eff}} \quad (25)$$

The parameter V_{eff} is the effective volume of the resonant mode. $Q = \frac{\omega}{\Delta\omega}$ is the quality factor as a ratio of the central emission frequency and bandwidth. $\frac{\lambda_c}{n}$ is the wavelength in the resonator media with refractive index n. The enhancement in spontaneous emission due to an increased LDOS of the cavity is frequently referred to as the Purcell effect or Purcell enhancement. The coupling of a quantum emitter to a resonant cavity is a powerful concept which allows us to tune the interaction of light and matter down to the single photon level. This notion has led to intense research allowing the study and testing of fundamental concepts of quantum mechanics in the area of cavity quantum electrodynamics. The ability to enhance a quantum emitter's emission rate while maintaining its pure quantum characteristics and strongly coupled and hybrid modes is of direct interest to the development of quantum information technologies.

Photonics cavity has an extremely high quality factor Q and high selectivity of the cavity resonance. To maximize the coupling strength, the most common photonic structure is the Fabry Perot resonator. To reduce the cavity size, the Bragg stacks or gratings, photonic crystal or microrings are developed. Such cavities, designed on the micro- and nanoscale, squeeze the mode

volume down to the diffraction limit. No propagating mode is available under the diffraction limit The dielectric material along is not able to get the task done.

Despite several demonstration of strong coupling in dielectric cavities, there are a couple of drawbacks makes the strong coupling a rare condition to be achieved[55]. First, the coupling strengths is restricted by the mode volume due to the diffraction limit. The optimized geometry cannot increase the photon output or brightness. Secondly, the coupling strength is an overlap function of the cavity and emitter, which is hard to match unless at low absolute temperature. Namely, the emitter spectrum should be narrow enough to match the cavity resonance.

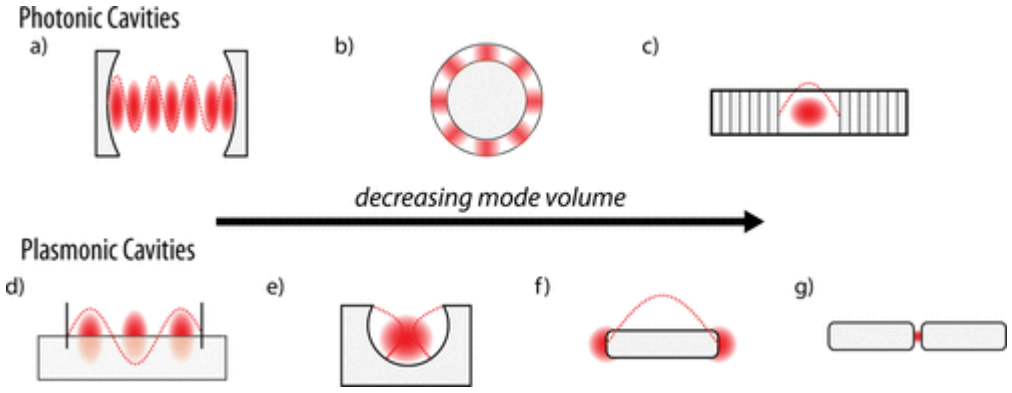

Figure 7: Sketches of photonics cavity and plasmonic cavities: (a) light trapped between two mirrors, to more sophisticated dielectric only options (to reduce metal losses), such as (b) microresonators and (c) micro-Bragg stacks or photonic crystals with defects; (d) trapped standing wave-type surface plasmon polariton cavities (e) with localized modes in nanocavity, (f) the dipole antenna and (g) gap plasmon. Reprint from ref[38]

Compared with photonics cavity, the plasmonic structure has a modest Q factor but is compensated with a cubic nanometer volume. The Purcell effect is thus amplified by the mode volume of the plasmonic cavity. It is possible to achieve strong coupling with the nanosize plasmonic structure[56]. On the other hand, due to the lossy cavity, the bandwidth of the plasmonic nanoaperture is on one order larger than the photonic cavity. The week coupling is more efficient in the plasmonic nanoaperture.

Weak coupling regime

Coupling by definition is to transfer the energy from one resonator to the other. The coupling in photonic system is the interaction of the two oscillators that involves scattering, absorption, and heat loss. The first resonator is a photonic cavity or a plasmonic cavity while the second oscillator is a two-level system (an atom or a quantum dot).

Weak and strong coupling are the scenarios of the light-matter interaction that can and cannot fit in perturbation approximation. In weak coupling regime, the energy transfer from the resonator to the other but the two-level system radiatively decays. The energy transfer is nonreversible and lossy. The coupling rate is stronger than the two-level system but is not strong enough to overcome the decay rate of the cavity resonator. The energy has a highly fast and one-direction flow. This regime is helpful to maximize the quantum efficiency of the quantum dots and maximize the brightness of the emiters. On the other hand, the strong coupling requires a coupling strength surpasses the cavity loss. The energy flow is fed back to the cavity and form a loop of the energy to compete with other decay rates. The application of the strong coupling are quatum circuitry and nanolasers.

Quenching

When a fluorescent emitter is close to a metallic surface, the emitter starts to lose its brightness. The non-radiative channel competes with the radiative channel and causes a quenching of the emitter despite of the high optical LDOS. This happens to both the flat metallic surface and metallic particles. In reality, the quantum emitter is barely a two-level system. The light is normally couples to radiative bright mode on resonance. Instead, the coupling excites the higher-order dark modes, losing energy to ohmical heat. The mode volumes of the plasmonic systems are very small

to enhance the coupling strength. The distance of the emitter should be less than the decay length of the plasmonic field, usually tens of nanometers. Instead of the enhanced spontaneous emission in Purcell effect, in this system, the quenching process dominants as the coupling strength increased with the decreased plasmonic mode volumes. The stronger coupling results in the absorption of non-radiative dark mode and the light output is drastically reduced. The measurement of the photoluminescence is hard to be detected. therefore, the detection of the strong coupling of this system is of plasmonic scattering spectra. By modulating the coupling strength, the emitter intensity is easy to be controlled in quantum computing. Some research suggests that the coupling between the plasmonic resonator and the quantum dots is able to modify the lifetime of the radiative mode. The plasmonic mode obtain teraherz decay rate fastening the lifetime of the quantum dots, which diminishes the blinking effect in quantum dots.

Nonradiative Decay Channels in Emitters

The quantum emitter might have several absorption channel instead of an ideal two-level system. Apart from quenching to the metal, the emitter has internal nonradiative decay channels and the radiative ones. Through internal conversion, a molecule can decay to the ground state without photon emission. This kind of internal conversion form a triplet excited state. Due to the golden rule, the transition from the triplet back to the singlet ground or excited state is forbidden. Herein, the lifetime of the triplet is as long as micro to milli seconds. The quantum dots in the dark state is called blinking and loses its quantum yield. This could heavily impede any useful application.

Fano resonance

Damping is originated from the ohmic losses or scattering losses due to the coupling to other modes. Here the frequency is a complex of the original central frequency and linewidth of the cavity. The imaginary part is the phase of the oscillators. The interaction between the oscillators leads to the shift of their eigenfrequency (a complex quantity has phase). The real part of this frequency shift is the emission frequency shift while the imaginary part represents the Purcell effect which modify the spontaneous emission rate in the cavity. Now assume one of the resonator 1 (cavity) has a larger damping and is driven by the external field. The corresponding linewidth of the spectrum is very broad relative to the undamped emitter, therefore, serving as a continuum. The phase of the undamped emitter changes by π at the resonance while the strongly damped cavity has slow phase change. Coupled spectrum of the cavity shows asymmetry with a dip and a peak as shown in Figure 8: sketch of the Fano resonance

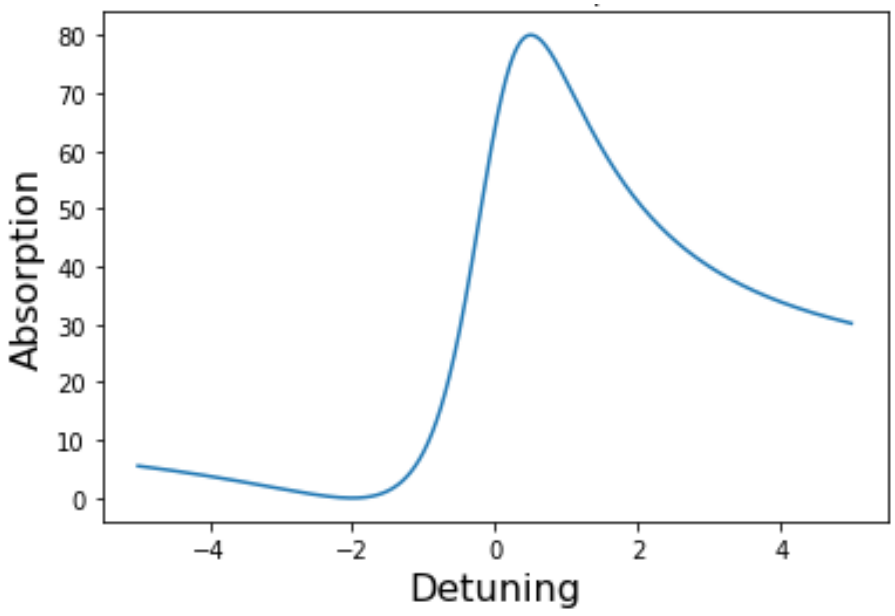

Figure 8: sketch of the Fano resonance

The two oscillators can be regarded as the interference of the two waves from the two oscillators. Damping induces absorption along with a phase delay. At the antiphase wavelength the cavity behaves a dip in the emission spectrum of the cavity; This phenomenom can be observed in photonics cavity and periodic structure to correct the Purcell effect.

Exciton-polariton

Polariton is formed when the optical excitation coupled with the matter excitation. The electrons, excitons, phonons and plasmons of the matter excitation (depends on the materials) oscillate following the optical electromagnetic field. For example, TM wave (magnetic field parallel to the interface) around the interface excites the collective excitation of surface plasmonic polaritons along the metal-dielectric boundary. The evanescent field extends perpendicular to the interface. Due to the high dispersion and high loss of the metal, these polariton modes are much smaller than the wavelength but extremely high local density of optical states, leading to strong light-matter interaction.

The condition of the excitation of polariton is not only limited to the metal but also the material with a negative permittivity[57]. The negative permittivity refers that the electric displacement vector has the same direction as the electric field vector. It is a simplified model noted in John Hopfield's paper as 'excitonic polarization', a mixed excitation mode of both matter and photon[58]. This model is very useful to describe the light-matter coupling in quantum dots and photonic cavities. For the polariton at semiconductor and dielectric interface, the excitons (electron and hole pairs), other than electrons, provides the oscillation with the photons. The external EM wave induces the optical absorption process and triggers an allowed electric dipole

transition. The excitons in the intrinsic QD state is created from the filled valence band. These are called as exciton-polaritons. Their similar behavior to plasmonic-polariton in metal suggests a negative permittivity of the free carriers and following a strong absorption of photons[59]. However, the exciton state is not necessary related to the radiation[110]. The exciton excitation might includes the phonon-assisted process and hence nonradiative Auger recombination.

CHAPTER THREE
SIMULATION

Finite element method (FEM)

Many engineering phenomena in stress, heat transfer, fluid flow and electrostatics can be expressed by a governing differential function and the boundary conditions. FEM is a method using spatial discretization to give approximate solutions to partial differential equations. It cuts the structure into several elements and connects the element at nodes as shown in Figure 9. The field quantity can be interpolated by a polynomial over the elements. The process creates a set of simultaneous algebraic equations. The adjacent elements share the degree of freedom at the connecting node. The complex mathematical problem can be simplified to a linear problem.

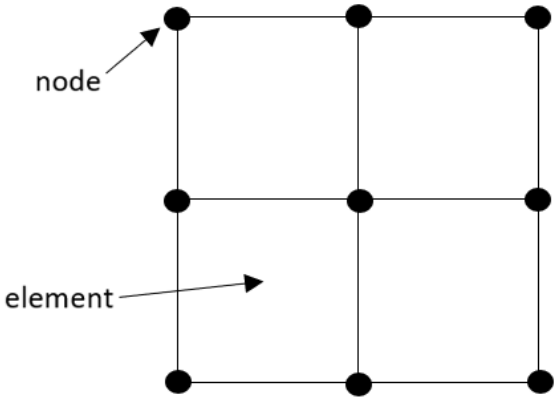

Figure 9: sketch of meshing in the FEM method.

In this study, I use COMSOL 5.3 commercial packet, which is a full-vector modal solver based on the finite element method (FEM). Instead of solving the partial differential equation of the Helmholtz function, a test function in Hilbert spaces is multiplied to both sides of the equation and the equation is integrated over all the domains. The weak formulation is obtained by requiring

this equality to be true for all test functions in the Hilbert space. It only requires in an integral sense rather than in all points in the partial differential equation. After that, an approximate solution to the weak formulation equation is expressed as a linear combination of a set of basic functions that belong to a finite-dimensional subspace to the Hilbert space. After substituting it into the equation, we get the discretized version of the equation, which contains a set of equations of the same dimension as the finite-dimensional function space.[48] The set of basic functions can be selected such that each of them has a triangle shape and is 1 at certain node and 0 elsewhere. Thus, the integrals in the discretized equation are nonzero only if the functions overlap, which leads to a sparse matrix for the set of equations. Boundary conditions are applied to solve this linear system of equations using linear algebra.

The continuum is diced into a number of elements. Those elements are mapped in the topological order, which is called meshes. The total number of nodes is $N_{nodes} = N_{elements} + 1$ for linear elements. It may be necessary to have extra nodes inside each element. Those elements is not necessarily of the same length. The accuracy depends on the size of the mesh. The calculation time is accordingly increased with a larger mesh number. To optimize the mesh distribution, it is better to follow the physics and the geometry as a non-uniform mapping[60].

Model and method

Wavelength

For many applications involving nanoapertures, it is important to find the antenna geometry that has the highest near-field enhancement at the working wavelength. The spectrum of the near field enhancement lines up with the transmission spectrum of the aperture. Since in an experiment

one measures the transmission through the nanoaperture this paper will focus on maximizing the transmission resonance. In order to increase the SIBA trapping potential at 1064 nm and 1550 nm, the optical resonance peaks of the nanoapertures should be close to the target laser wavelength. Specifically, for SIBA trapping the resonance peak of the antennas should be blue shifted from the excitation wavelength. This is because once a nanoparticle is trapped, the transmission peak is red-shifted for particles with positive polarizability [61]. Therefore, optical trapping with a 1064 nm and 1565 nm laser should have nanoapertures whose geometries are optimized to have un-trapped native transmission resonances at 1050 nm and 1550 nm respectively.

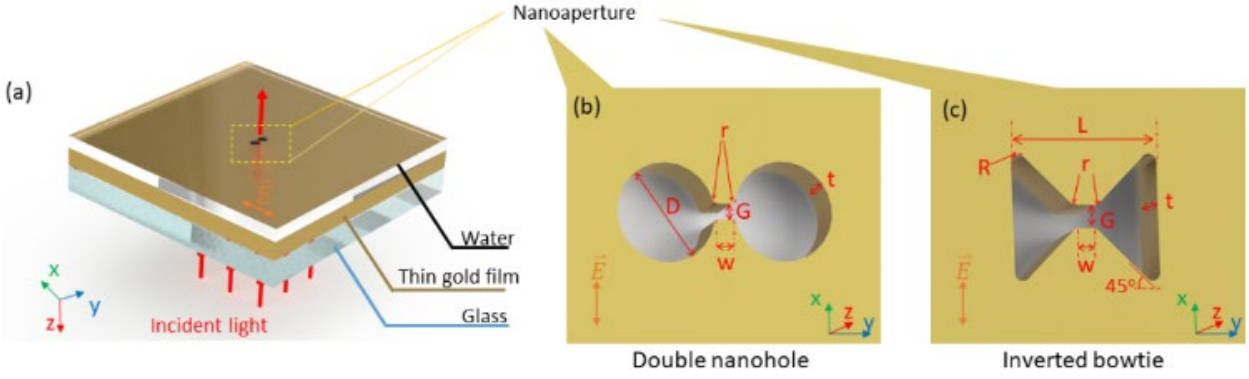

Figure 10: (a) the 3D geometry of the simulation layers; two different design of nanoapertures: (b) Double nanohole with parameters: corner radii r, gap size G, edge-edge distance of the two holes W, the diameter of the holes D, the thickness of the film t; (c) Inverted bowtie with additional sweeping parameters: inner corner radii R and outline parameter L.

Geometric Design

The schematic of our sample is a multilayer structure as shown in Figure 4. The material stack used in the simulation starts with glass followed by the metallic layer with the nanoaperture and then water, with water also filling the void of the nanoaperture.

Each layer is parallel to the XY plane for this simulation. The refractive indices of water and glass are set to be 1.33 and 1.52 respectively. A monochromatic plane wave propagates along the z axis from the glass side. The long axis of the nanoaperture is along the y direction. Since the

structure of the aperture is not centrosymmetric, the polarization of light perpendicular to the long axis of the aperture has a larger local field enhancement than parallel to long axis [62]. Thus, the polarization of the incidence is along the x axis.

Structure of the nanoaperture

We mainly compare two different structures, inverted bowtie and double nanohole (DNH) as shown in Figure. 1. The inverted bowtie is mainly characterized by the outline parameter L and gap size G. The angle of the corner of the bowtie is chosen as 45^{o} due to the results by Qiao et al [63]. The DNH is characterized as the diameter of the holes, the gap size G and the edge-edge distance between the two holes. Expanding on other simulations[64] , the corner radius r of the gap region and R of the inner corners for the inverted bowtie are also taken into account. These corner radii are important and due to fabrication limitations, there can be a smoothing effect of the corners. The corner radii of both structures are always kept to 2nm if not specified.

The simulations start with a 100 nm thick gold layer or an 80 nm thick aluminum layer as the material for the film. These materials were chosen for their high absorption coefficient, prevalence in plasmonic based devices, and ease of fabrication. It has so far been standard practice to use thin gold film for its low loss, convenient functionalization process [65], biocompatibility and temperature stability in visible and NIR wavelength range [61, 62, 66]. Similar to gold, aluminum is biocompatible and durable [67], it may be seen as a less expensive material for use in nanoaperture optical traps. Moreover, aluminum naturally is coated with a thin layer of oxide which protects the layer from contamination and is easy to clean. The refractive index of gold and aluminum are taken from the interpolation of data from Johnson and Christy [68] and McPeak [69] respectively. Table 1 shows the thicknesses of gold and aluminum films we choose for our design

and the transmission of the films. The thickness of the aluminum layer is smaller than gold layer due to its larger imaginary refractive index k. A thinner layer is preferable because it is easier to fabricate nanoscale features than in a thicker film. The major part of design is based on the gold material and we will compare gold and aluminum nanoapertures at the end.

Table 2: Optical constants used for gold and aluminum

Wavelength (nm)		1064	1565
Au	Real part of refractive index n	0.258	1.029
	Imaginary part of refractive index k	6.965	9.252
	Transmission (100 nm film)	2.59e-04	1.59e-04
Al	Real part of refractive index n	0.533	1.368
	Imaginary part of refractive index k	10.859	14.272
	Transmission (100 nm film)	3.17e-05	4.87e-05

Simulation model

The simulation tool is COMSOL Multiphysics, a finite element method (FEM) software program. The boundary conditions used are perfectly matched layers (PML). The simulation volume is set to be big enough to avoid artifacts (6 times the aperture size in XY plane and 3 μm in both the negative and positive z directions). All the simulation domains are meshed using tetrahedron except the PML which uses swept mesh. The minimum mesh size for the simulated geometry is less than 3 nm. A probe is placed in the center of the geometry to get the near field enhancement $\left|\frac{E_x}{E_{in}}\right|$ (E_x is the electric field along x direction in the center of the aperture and E_{in} is the incident electric field) and the transmission is measured at the far field after the aperture. Since these nanoapertures utilize near-field enhancement, only the plasmonic peaks (0th order peaks) are considered.

Simulation results

Polarization simulation

Due to the non-centrosymmetric geometry of the DNH, the nanoaperture has a polarization direction preference. The transmission remains the maximum when the polarization is aligned to short axis (across the gap area). The minimum transmission is at the direction along long axis of the DNH.

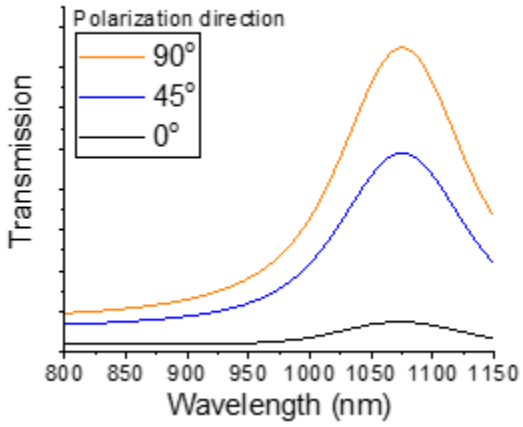

Figure 11: simulation spectra of a DNH aperture with an incidence of different polarization direction. The polarization direction 0° is aligned to the short axis of the DNH.

Inverted bowtie nanoapertures

We first optimize the structure of the inverted bowtie. All the inner corner radii are kept as R = 1nm. For convenience, we set the gap area as a square with its length G equal to its width W. The transmission of the light is defined as the ratio between the transmitted power of the far field with and without the aperture. For a smaller gap size, the outline length of the aperture must decrease accordingly to maintain the same frequency resonance[70]. Due to the asymmetry of the geometry, the nanoaperture is sensitive to the polarization of the incidence. With a polarization perpendicular to the long axis of the aperture a smaller gap size will result in a stronger coupling

across the gap between the metallic cusps and a higher near field enhancement. This stronger field is repulsive to the incident field, leading to a lower resonance frequency whereas the outline length of the aperture is shortened (along the long axis) to compensate the resonance frequency[37]. As shown in Figure 5(a, d), with the polarization perpendicular to the long axis of the aperture, the larger gap sizes lead to higher transmission. On the other hand, the optical enhancement within the center of the gap decreases as the gap size increases. Figure 5(c, f) shows the near field electric field profile in the center of the aperture. Actually the maximum near field enhancements are not exactly at 1550 nm when optimizing the transmission peaks at 1550 nm[71]. However, since the differences between the peaks of near field enhancement and far field are less than 5 nm, the near field pictures of 1050 nm and 1550 nm are shown. These show the near field enhancement is large at the center of the inverted bowtie. Moreover, the nanoaperture with a smaller gap and a smaller gap width results in a smaller transmission bandwidth. This can be explained by the quality (Q) factor of the cavity. The Q factor is inversely proportional to the transmission bandwidth of the cavity. The surface area of the gold cavity is smaller when decreasing the length of the nanoaperture, therefore the loss is lower. Furthermore, as the confinement increases the resulting bandwidth decreases. Here, we refer to transmission bandwidth rather than near field enhancement. For surface enhanced fluorescence or Raman spectroscopy, the near field enhancement and Q factor are important figures of the merit to characterize the near field signal[72]. However, self-induced back-action trapping does not rely on the gradient force to trap particles, as a result a strong resonance, but not a strong near field enhancement is required. The optical characteristics of the nanoaperture is based on its geometry, which in turn determines the profile of the transmission resonance[73].

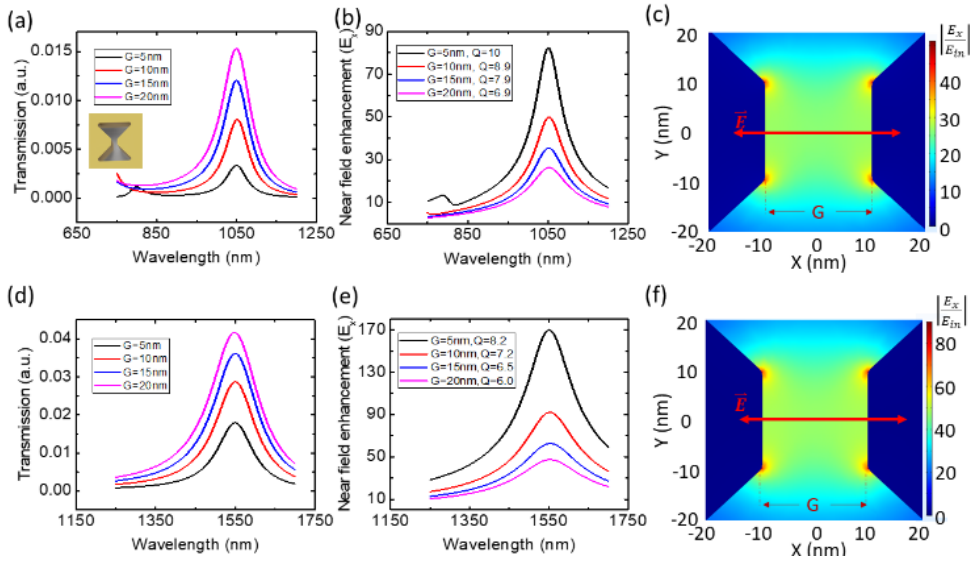

Figure 12: Transmission, near field enhancement spectra and field distribution of the optimized inverted bowtie structure for transmission peaks at (a-c) 1050 nm and (d-f) 1550 nm. (a) Transmission for 1050 nm inverted bowtie with different gap size G. (b) Near field enhancement for 1050 nm inverted bowtie. (c) The near field enhancement profile for nanoaperture resonating at 1050nm with a 20nm gap size. (d) Transmission for 1550 nm inverted bowtie. (e) Near field enhancement for 1550 nm inverted bowtie. (f) The near field enhancement profile for nanoaperture resonating at 1550nm with a 20nm gap size.

Any change to the nanoaperture geometry, including a trapped nanoparticle, will change the transmission resonance. When measuring SIBA trapping, detection of the transmission in the far field is enough to accurately measure the trapping event. It is easy to misunderstand the role of the near field optical enhancement which enhances the gradient field and therefore would result in higher gradient force trapping. However, SIBA trapping does not utilize this enhancement as the trapping mechanism[74]. As shown in Figure 5 and Table 3, the optimized outline length of the bowtie L is kept to 106.5 nm for 1050 nm structure and L = 188 nm for 1550 nm structure. The gap size G are 20 nm for both wavelengths.

Table 3: The geometries of inverted bowtie structure after optimization

Gap size W (nm)	Outline length L for 1050 nm geometry	Outline length L for 1550 nm geometry
5	72.5	148.5
10	88.5	167.0
15	98.5	179.0
20	106.5	188.5

Due to the limitation of fabrication techniques, the four internal corners of the inverted bowtie structure are barely sharp enough. For example, helium FIB technique can give less than 2 nm radius with 0.35 nm resolution [75] while with a gallium FIB one can obtain a radius of 5 nm [61] in ideal conditions. Therefore, in this part, we first study the corner effect of the inverted bowtie structure. The inner corner radius is swept from R = 2 nm, R = 6 nm, and R = 10 nm. The results show that larger inner corner radius leads to a blue-shifted of the far field resonance wavelength and slight decrease in transmission. The resonance peak shifts 45 nm when changing the bowtie radius by 4 nm for the 1050 nm structure. In the same case, the near field enhancement dips from 26 to 18 when increasing R from 2 nm to 6 nm. Therefore, the inverted bowtie structure is very sensitive to the fabrication resolution due to the four internal corners. Thus, we want to compare this geometry to a double nanohole which will have an easier process for precise fabrication.

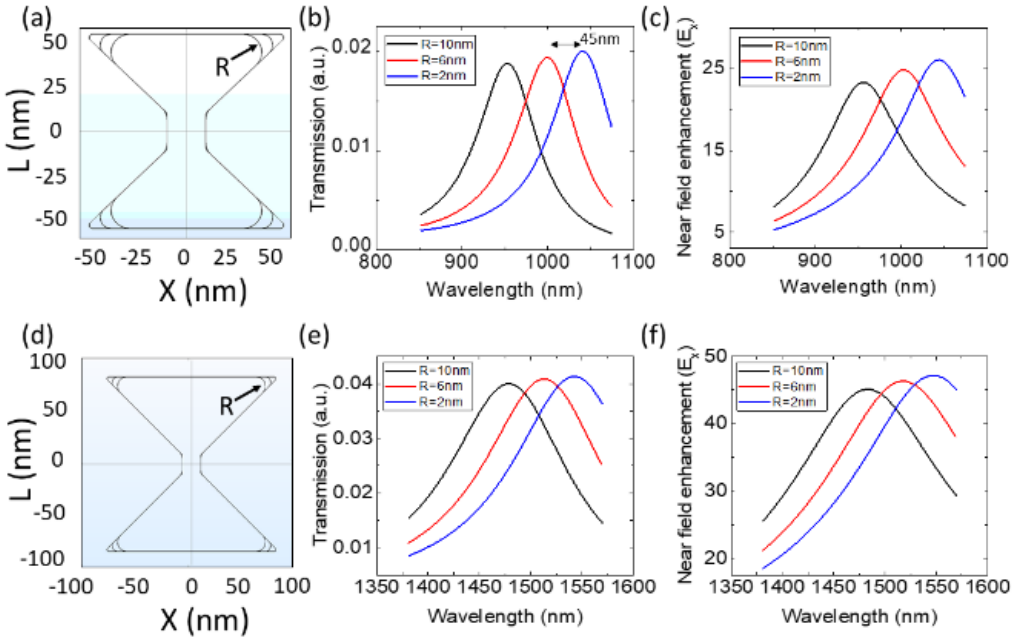

Figure 13: Internal corner effect of inverted bowtie structure. (a) Geometries of 1050 nm structure when R=2nm, 6nm, 10nm. (b) Transmission spectra and (c) near field enhancement of 1050 nm inverted bowtie structure of different inner corner radii while L = 106.5 nm. (d) Geometries of 1550 nm structure when R=2nm, 6nm, 10nm. (e) Transmission spectra and (f) near field enhancement of 1550 nm inverted bowtie structure of different corner radii while L = 188 nm.

Double nanohole nanoapertures

Compared with the inverted bowtie, the DNH structure is easier to fabricate because there is no need to consider any internal corners. Figure 7 shows the transmission and near field enhancement curves after optimization. Table 3 shows the geometries after optimized for the specific wavelength. The gap sizes G of the nanoapertures are set as 5 nm, 10 nm, 15 nm, 20 nm which are reasonable and plausible for nanofabrication [76, 77]. The bigger the gap size is, the more the peaks shift to a shorter wavelength. This phenomenon agrees well with Qiao's research [63]. One of the most important factors is the peak height of the near field. When optimizing the peak position at a specific wavelength, the center frequency is higher for the smaller gap. From Figure 7, one can compare the near field enhancement of the structure at two different wavelengths.

Comparing these two wavelengths, the near field enhancement of 1550 nm structure is two times larger than that of 1050 nm structure. This implies the potential for greater trapping strength.

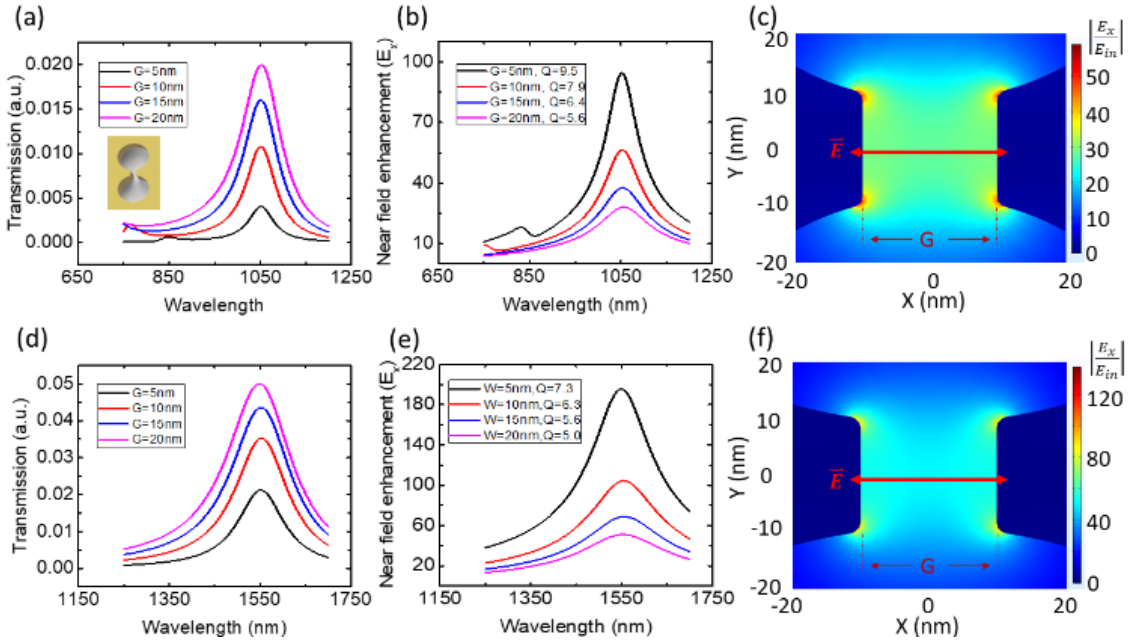

Figure 14: Transmission and near field enhancement spectra of the optimized DNH structure for transmission peaks at (a-c) 1050 nm and (d-f) 1550 nm. (a) Transmission for 1050 nm DNH. (b) Near field enhancement spectrum and (c) field distribution for 1050 nm DNH. (d) Transmission for 1550 nm DNH. (e) Near field enhancement spectrum and (f) field distribution for 1550 nm DNH.

Table 4: The geometries of optimized DNH structure

Gap size W (nm)	D for 1050 nm geometry	D for 1550 nm geometry
5	53.0	109.0
10	62.5	119.0
15	68.0	124.5
20	72.0	128.0

Previous simulation process steps set the gap size and gap length as the same. Here, we also investigate the gap length as a parameter for the structure resonance. As shown in Figure 8, the scale bar is shared by both (b) and (c). A red shift of the wavelength results from a larger edge-edge distance W of the two nanoholes. The electric fields of resonance wavelength have large

enhancement around the gap area. however, for different length of the edge-edge distance, the electric field enhancement does not change much.

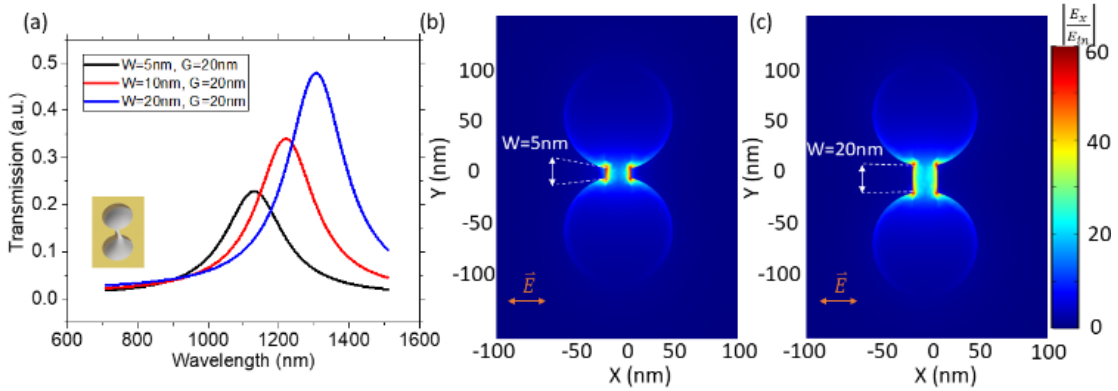

Figure 15: (a) simulation spectra with different edge-edge distance of the two nanoholes W; the normalized electric field distribution when (b) W=5nm, (c) W=20nm with both figures share the same legend on the right.

To further compare the two structures, two main factors are considered as shown in Table 5. The first is the near field enhancement. The near field enhancement of the inverted bowtie is comparable to that of the DNH structure. The second is the full width half maximum (FWHM): the FWHM of the inverted bowtie is also comparable to that of the DNH. As a result, the DNH is an acceptable alternative to the inverted bowtie structure with the fabrication of the DNH being much easier and less sensitive to error.

Table 5: Comparison between the near field enhancement and FWHM of DNH and inverted bowtie

Gap size W (nm)		5	10	15	20
DNH structure	Near field E_x at 1050 nm	94.4	56.2	37.5	27.9
	FWHM 1050 nm (nm)	111.0	133.0	163.5	186.0
	Near field E_x at 1550 nm	195.7	104.3	68.7	51.1
	FWHM 1550 nm (nm)	211.5	247.0	278.5	306.0
Inverted bowtie structure	Near field E_x at 1050 nm	82.3	49.7	35.4	26.2
	FWHM 1050 nm (nm)	105.0	118.5	133.0	153.0
	Near field E_x at 1550 nm	169.9	92.0	62.7	47.4
	FWHM 1550 nm (nm)	189.0	214.5	238.0	257.5

Nanoaperture with nanospheres

The NAOT employs the SIBA theory, where the nanoparticle induces a red shift of the resonance spectrum. In our simulation shown in Figure 9, the 20nm gold nanoparticle shift the resonance spectrum of the nanoaperture by 90nm. In the figure, the situation with an incident laser beam wavelength in the pink section is defined as red-shifted region, where the transmission decreases after trapping. In the blue section means the transmission will increase with a wavelength larger than 1210nm, named blue-shifted regime. At the interception point of the two spectra, the transmission does not change its amplitude once trapped.

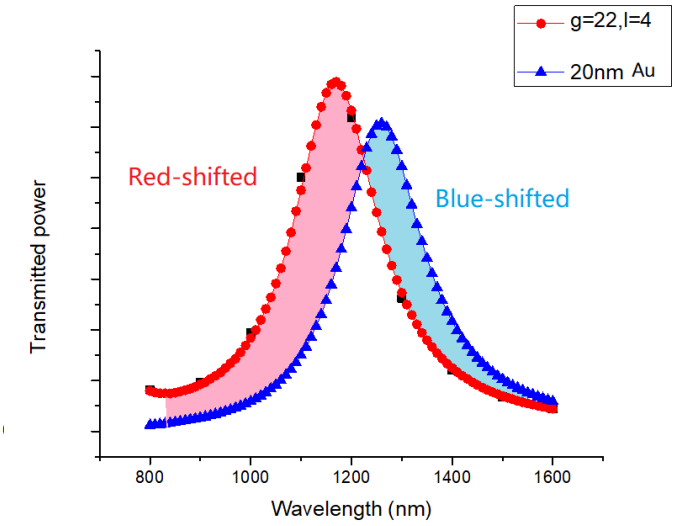

Figure 16: simulation on the transmission spectrum for 1064nm aperture with 22nm gap size (red) and an aperture with a 20nm-diameter gold sphere

Nanoaperture with nanorods

In the previous sections, spherical particles in a nanoaperture are simulated. However, most of natural particles are inhomogenous in shape. Therefore, the study of elongated particles is necessary. This sets a foundation of the orientation analysis for the following experiment of the elongated particles.

I used COMSOL to simulate the transmission spectra of a gold rod in a 22nm gap aperture resonating around 1330nm. The gold rod is 10nm in diameter, 20nm in length. As shown in the Figure 12, empty cavity (the black dash line) and the nanorod at 125nm from the glass substrate (olive dot line) has the same spectrum. Namely, when the particle is over 5nm away from the metal-water interface, the coupling between the two is zero. The same red-shifted spectra appears at the presence of the nanorod inside the gap area at 62.5nm from the metal-glass interface (blue line). The orientation of the nanorod behaves differently along x,y and z axes.

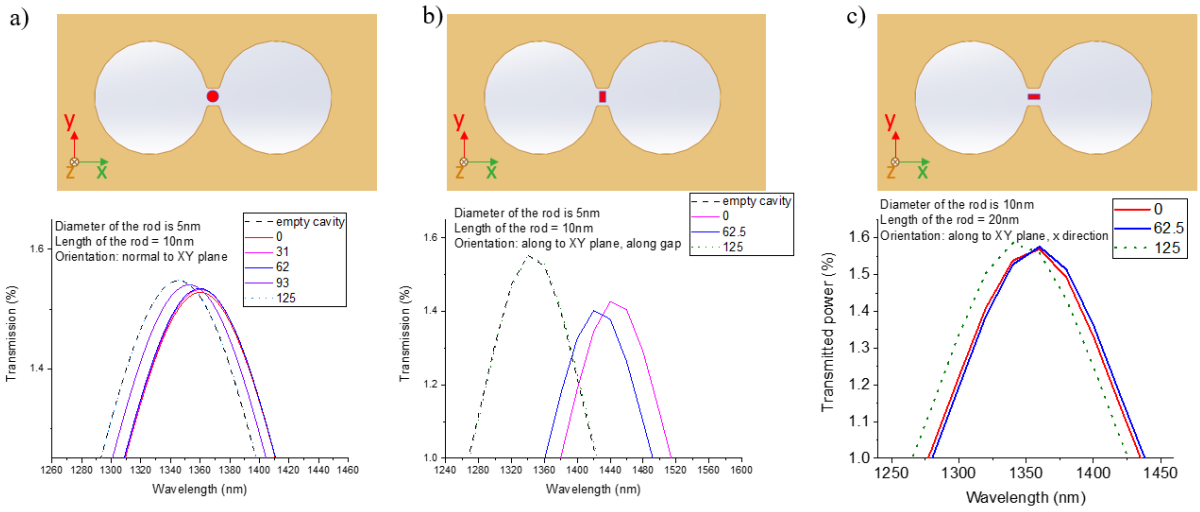

Figure 17: the sketch and the simulated transmission spectrum of DNH with a nanorod orientation a) along z direction, b) along y direction and c) along x direction. The different colored spectra represents different nanorod position in the gap area where 0 is at glass-metal interface, 100 is at water-metal interface, and 125 is in the water region above the metal.

When the particle is oriented along z direction, the presence of the nanorod redshifted the transmission spectrum. The center of the spectra is not significant changed when the particle is at 0nm, 31nm and 62nm. When the particle moves closer to the metal-water surface (at 93nm), the spectrum is shifted less than the ones close to the glass-metal interface. The spectrum is very sensitive to the position of the particles. Compare the blue line (62nm) Figure 12 a) and b), the

spectrum shifts more with a y-axis (from 1340nm to 1430nm) oriented nanorod than the z-axis oriented (from 1340 to 1360nm). The x-axis orientation shows the same number of spectra shift as the z-axis orientation. The strong field between the nanorod and the gap is significantly squeezed when the particle is in the y-direction. The coupling in the system is much strong than the other two cases. Therefore, the DNH is able to recognize the orientation of the nanorod by measuring the transmission spectrum.

CHAPTER FOUR:
NANOFABRICATION

In our daily life, nanostructures are widely spread in our daily life, such as the information storage on silicon integrated circuit chips, display, telecommunication, 3D printing, vaccine and etc. All these products rely on the stability and reliability of nanofabrication technology in synthesis and characterization. With the development of the nanofabrication, it becomes possible to manipulate atoms and program the structures and surface properties. Those fabrication methods to generate the nanostructures are categorized in the top-down (reactive ion etching, electron beam lithography) and bottom up (self-assembly, self-organization) fabrication process. The top-down method uses lithography to carve the nanostructures out of the substrate[78]. On the other hand, the bottom-up method uses molecule interaction or colloidal particle to self-assemble the discrete nano structures in two or three dimensions. This method works well for the periodic geometry in thin films. It can be applied to mass production by making a mask and stamping the geometry duplicates continuously.

To reach the consistency of the fabrication and design, the main challenges in the project are the sub-10nm lateral resolution of the geometry and the material property improvement. This sub-1nm resolution has received much attention due to the development of the plasmonics study. The scalability, controllability and reproducibility of the fabrication are essential in fabrication efficacy. In lithography, the lateral resolution is declined due to the increase depth (or height) of the feature. The simulation-fabrication consistency helps the accuracy of the following experiments. Furthermore, in different fabrication process, the material might change its properties due to the existence of the intrinsic strain, grain size and morphology. In this chapter, I would like

to introduce some top-down nanofabrication process to set a foundation for the NAOT and other plasmonic devices.

Physical vapor deposition

The fabrication process for manufacturing nanoapertures requires the deposition of a thin film of metal onto a glass substrate. Epitaxial growth is the deposition of a layer of material that preserves a particular crystallographic orientation. The orientation of the lattice during the deposition process is affected by the substrate temperature, the orientation of the substrate[79], lattice misfit of the coating material and substrate, etc.[80] Physical vapor deposition (PVD) usually consists of thermal evaporation, electron beam evaporation and sputtering. On a single crystal substrate, a lot of researches succeed in growing crystals with parallel epitaxy and form a large single crystal with sufficient care and control[79]. However, due to the atom mobility and the surface tension, random orientation and rotation of the(material).

Gold particles have significant diffusion at the surface of the Si and Ge substrate[81]. As for thin film less than 30nm, gold islands are prone to cluster together without proper control of the substrate and environment control. With the increase of the thickness of the film, the edge of the islands touches with each other. However, due to the orientation, the mismatch of the boundary forms defects and results in polycrystalization. Fast sputtering is able to obtain a small grain size of less than 20nm in diameter[82]. Thermal evaporation, without substrate temperature control, results in 30nm for average grain size.

Annealing

Twin grain is the grains that is a reflected image of its neighbors or is rotated with respect to it during the intergrowth. The individuals usually comprise a twin have atomic structures with different orientations, but they have certain common planes or directions.

Twin grains are divided into two main categories, annealing and mechanical twins. The defects of the grain boundary are low-energy boundary. It can be mitigated by energy introduction, such as elevated temperature or pressure. These two factors vary the atom diffusion, modify the boundary orientation and coalescence the grain. The method is so called annealing.

At the same time of increasing grain size, annealing causes surface roughness and wetting problem of the exposed side of the coating material.

Grain size and optical property

Crystallographic factor is an important constant for lattices structure, such as milling rate, thermal dynamics and conductivity of the material. The propagation of EM field is based on the behavior of the local electrons. The grain and the surface roughness affect the propagation of the electrons due to the scattering at the boundary. Thus, the grain size affects the resistivity of the thin film[83]. However, if the electron is not affected by those material defect, namely when grain size is much larger than mean free path (scattering happens), the microscopic scale is comparable to the bulk material[84].

Focused ion beam

The lithography is the key patterning procedure in nanofabrication. Focused ion beam is a kind of scanning beam lithograpy. It was first proposed by Feynman around 1959 but is realized

in 1973 by Seliger and Fleming[85]. Compared to photolithography, it is slow and expensive. But the biggest advantages of the FIB are its straight-forward use that can mill almost any conductive material and has high spatial resolution[86, 87]. A relatively new FIB has been developed that uses helium and neon ions that can mill with much higher spatial resolution and control[88, 89]. This tool has enabled the fabrication of new nanoscale devices with even smaller feature sizes.

Ion source

The most common ions in FIB, from light to heavy, are He^+, Ne^+, Ga^+ and Xe^+. The bombardment of ions transfers the kinetic energy to sample material surface. The ion etching are widely used in industry for microfabrication (i.e. reactive ion etching and ion implantation). It was not until the discovery of liquid metal ion sources (LMIS). Under a strong electric field (high extractor voltage around 30keV), the metal heated up to the liquid phase is droped from a sub10nm tip. The 'droplet' has high surface tension emits ions instead of droplet. Then the ions are accelerated theough a column at voltages from 500V-50kV and got focused by electrostatic lenses. The ions are concentrated at a beam current around 1pA to tens of nA. Based on the LMIS source, FIB (of Ga^+) is capable of generating ion beam of tens of nanometer in size (keV)[90]. This LMIS source also works for alloy at its low temperature eutectic composition and obtain the liquid phase.

The Ga^+ FIB performs very well in both nano- and micro milling and deposition. However, it induces a lateral expansion. The resolution of the conventional galium FIB has a resolution limitation at 10nm. To solve the problem, a gas field ionization source (GFIS) is developed to usestable inert gases such as helium and neon. Those light mass ions has a beam size roughly 0.5~1.9nm, which is sufficient enough to fabricate sub-10nm features[91, 92]. Both of the methods

(GFIS and LMIS) suffers from spherical aberration that limit their efficiency in micro and macro-milling.

Ion-solid interaction

Ions with kiloelectron volt energies incident on a solid surface makes atom sputted off, electrons emitted, induces chemical reation and ion implatation. During the penatraion of the ions, energy is transferred to the target due to the ion-solid interaction.

To simulate the implantation of the ions, the stopping and range of ions in matter (SRIM) Monte Carlo simulations of ion trajectories and multiple scattering is developed. In the flight of the ions, it continuously lose energy to the interaction with electrons and nuclei. The the energy loss per unit pathlength is defined as 'stopping power'. The interaction with electrons are elastic while the one with nucleus is inelastic. The ions are assumed to be accelated by same energy 30keV. The interaction volume is propotional to the mass of the ions. The light mass ions, such as helium, is dominated by the electronic stopping while heavy mass ions by the nuclear stopping. Therfore, He^+ compared with Ga^+ has longer penertration length and less lateral surface scattering. For a thin film, the implantation of hellium is much less than neon and gallium. Hellium ion beam is premium in the imaging, nanomilling and nanodeposition resolution.

Fabrication results

Sample morphology

In the annealing process, the heat increases the lateral diffusion in the vicinity of the grain boundary. The silicon wafer has a native oxide layer, which prevents the distribution of gold vertically into the wafer and the formation of silicide[93]. Without using any adhesion layer

(titanium or chromium), the gold atoms are free to diffuse on the surface of the silicon wafer [94]. The first step is to evaporate gold onto a cleaned glass slide. After which it is then placed into a vacuum oven. The temperature is ramped up to a set maximum and held there for some time. It is essential to control the cooling speed to better affect grain growth and distribution. Quenching, the immediate cooling of the material, will result in a nanocrystalline structure as the tiny grains are quickly locked in place. However, by slowly cooling, the grains are allowed to grow, and areas of single crystal can be 100s of nm in size. As the temperature decreases, the lateral gold atoms modify their orientation and coalesce the separated small grains into larger ones. The higher temperature leads to better surface diffusion of the particles and more grains fusion, as shown in Figure 11. The typical temperature of gold film heat treatment is from 200 ºC to 550 ºC. The higher the temperature does give rise to larger grain sizes. However, nano-sized holes emerge while more material is required to fill the pitch and trench in between the grains. Those nano-pinholes are small at the exposure side but large at the buried side, forming a cone-shape in the film. In this case, the trade-off between large grain size and the following pinhole is essential in this process. Due to the size of our desired aperture, the annealing temperature is set at the range of 200~250 ºC where grain size reaches 500 nm with no nanoaperture. The grain size is much larger than the mean free path of the gold layer, suggesting the consistency of the dielectric function and electric resistance with the bulk material[84].

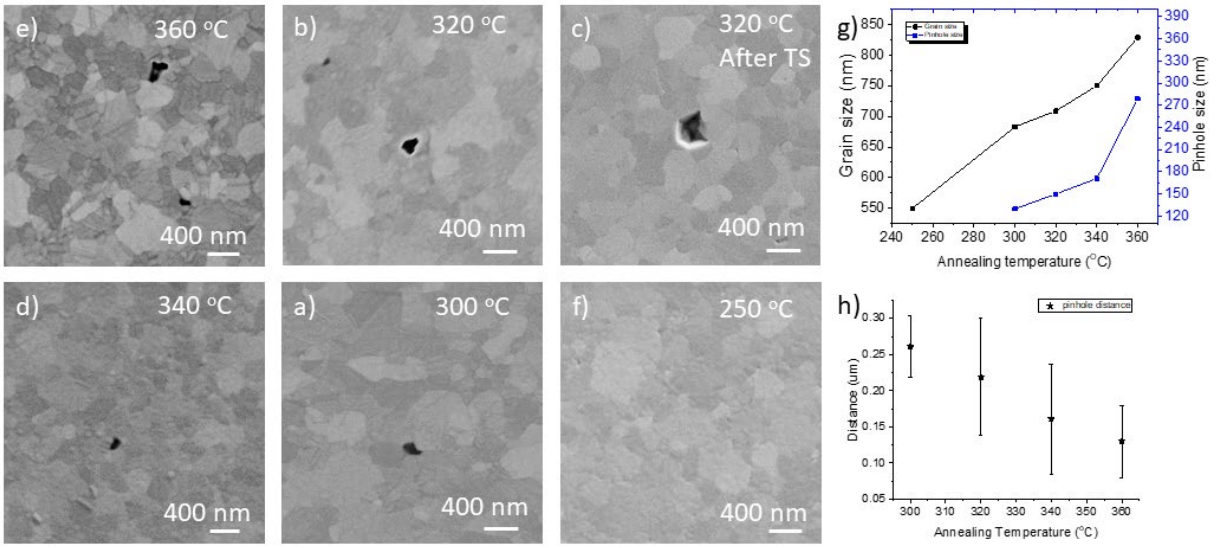

Figure 18 SEM image of grains and pinholes in gold film after annealing at temperature a) 300 ºC, b) 320 ºC, d) 340 ºC, e) 360 ºC, f) 250 ºC; c) cone shape aperture after annealing at 320 ºC and template stripping; g) diagram of grain size and aperture size vs. annealing temperature; h) diagram of pinhole distances v.s. annealing temperature. Reprint from [95]

As shown in Figure 12(a, b), the different orientations of grains are interpreted in different brightness by scanning electron microscopy. The annealing treatment induces orientation modification and fuses them. On average, the grain size expands from 20~30nm to 500nm in diameter after 2-hour annealing treatment in vacuum. Figure 12(c-f) is the surface characterization of the sample after template stripping. The result of the atomic force microscope shows that the unannealed sample has spike shape grains with a maximum height of 53nm. As a comparison, the deviation of the processed sample only ranges from 0 to 12nm. The average line roughness of the surface decrease from 1.52nm per line to 0.267nm per line. After the template stripping, the buried side of the gold film exposes. Because of the thickness of 100nm, the surface roughness is dependent on the surface cleaning and condition of the silicon wafer instead of the evaporation process.

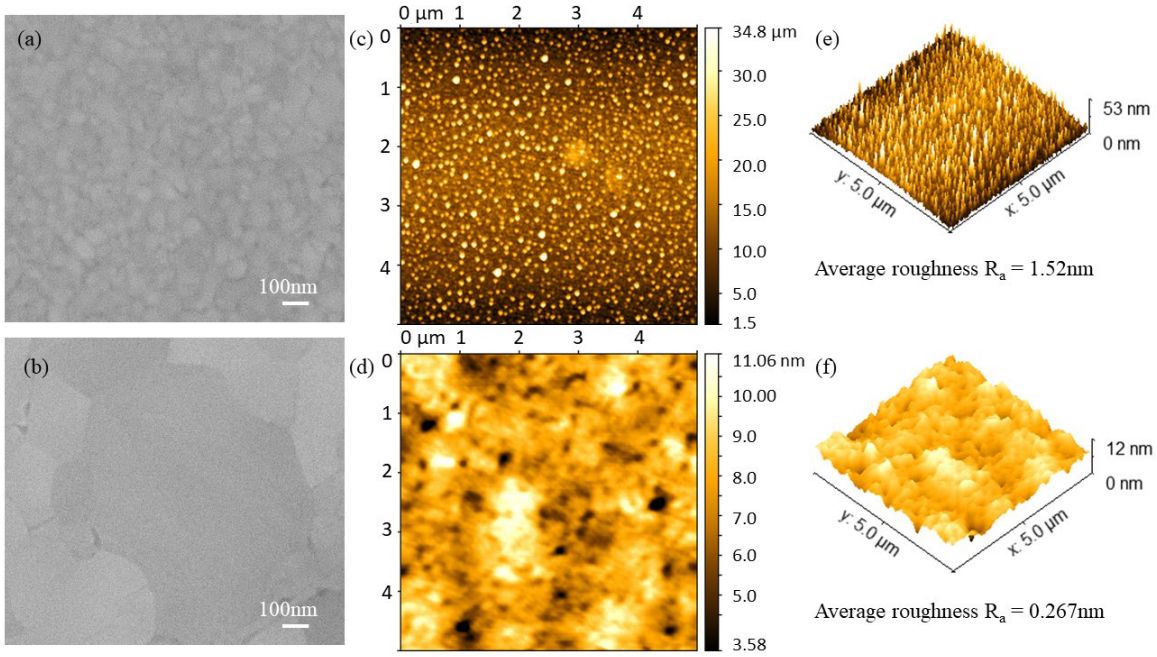

Figure 19: SEM image comparison of grain size on thermal evaporated samples (a) without annealing and (b) with annealing treatment at 310ºC for 5 hours; 2D roughness study with atomic force microscopy (c) on unannealed sample and (d) on annealed sample after template stripping; 2D roughness study with atomic force microscopy (e) on unannealed sample and (f) on annealed sample after template stripping. Reprint from [95]

Focused ion beam lithography

In this part, we compare the experimental results of the conventional Gallium FIB and Helium ion microscope (HIM). Artifacts are also arisen due to the heat effect of the high current beam[96]. In our experiment, the gold film plays a role in the heat and electron distribution, which eliminates the effects. The beam currents are both controlled under 7pA for high precision and low local heat effect. The dosage of the Gallium ion beam is 2.5 pA for 0.5 seconds. The dosage of the Helium beam is 7 pA for 8 seconds. The same beam energy 30keV is used to facilitate direct milling comparison. All the in-house samples in use are carefully prepared through the progress mentioned in section 3.1. The commercial samples are used to compare the effect of the grain boundary. These commercial samples are sputtered with 100nm gold film and adhesive layer Ti.

The grain size is around 20nm in diameter. The same geometry of the double nanohole (DNH) is set to observe the ion beam performance.

Without the perturbation from grain boundary, both gallium and helium beam are able to mill precise DNH geometry with a sub-20nm gap feature, as shown in Figure 13 (c, d, g and h). Since the long axis of the double nanohole is less than 200nm, the shape fits in a single grain, and the corners of the gap area are clear and sharp. However, HIM is more superior to Ga FIB in terms of consistency. The comparison between Figure 13(b) and (f) shows that the Ga FIB induces asymmetric deck area when the gap distance is down to 12nm. In contrast, the one fabricated with HIM remains straight edges. It can be explained that the conventional focused ion beam utilizes gallium liquid metal ion source to remove the target material while the HIM uses gas field ion source (GFIS) to create a sharper Gaussian beam[97]. Note the milling rate of the ion beam also performs slightly differently due to the orientation of the grain.

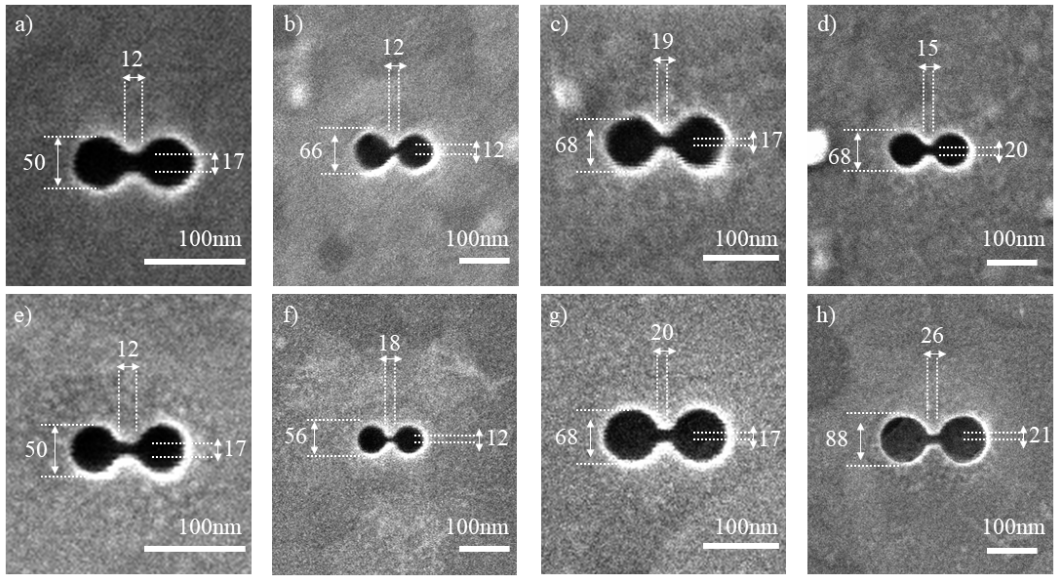

Figure 20: (a-d)SEM image of boundary effect on in-house annealed samples with Gallium ion beam and (e-h) HIM image of nanoaperture milled with Helium ion beam within a single grain. The gallium ion fabricated DNH has a visible effect of the round corner effect at the gap area and the asymmetric mutation of the two decks of the gap area.

As mentioned before, the dislocation of the grain affects fabrication precision. As shown in Figure 13(a), the grain boundary hits the gap of the double nanohole and the nanohole on the right. The nanohole is slightly elongated at the right end. In Figure 14(a and c), commercial samples with ~20nm grains show the shape mutation due to the grain boundary. The fabricated gap feature is even more than 20nm. Nevertheless, the asymmetric deck area and corner smoothing effect are also inferior to most of the in-house samples in terms of fabrication resolution. The strain at the grain boundary behaves differently based on the orientation and material of the grains on each side[98]. When the ion beam interacts with the grain and surface, the strain in the film leads to different mutations. In this case, our proposed sample preparation process does have a positive effect on the fabrication resolution.

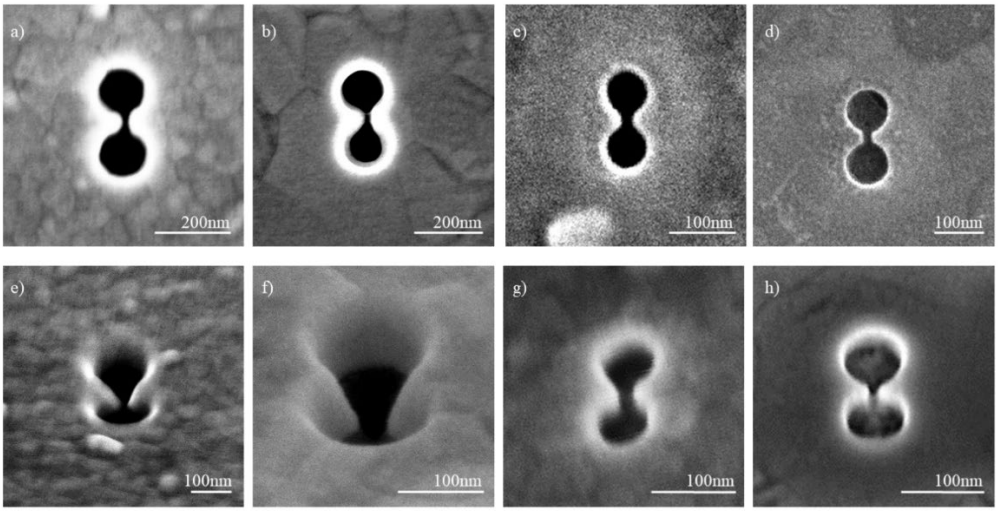

Figure 21: The top view and tilled view of the sidewall feature of the double nanoholes fabricated (a, e) on an unannealed sample with Ga ion beam; (b, f) on an annealed sample with Ga ion beam; (c, g) on an unannealed sample with Helium ion beam; (d,h) on an annealed sample with Helium ion beam.

We also investigate the sidewall of the double nanohole, which affects the optical property of the nanoaperture and plasmonic response mentioned in our previous work. In Figure 14(e and f), the cusps of the double nanohole fabricated by Ga ion has a slippery sidewall of approximately

53° and 61° angle. As a comparison in Figure 14(g and h), the HIM sample has a straight sidewall feature. It is explained by the longer stopping distance of the lighter ions (He^+). According to other researches on Monte Carlo SRIM simulation, the helium ions scatter much less than the tear-drop shaped gallium ion beam[99]. This lateral scattering simulation and experiments result by STEM-XEDS mapping propose a local thinning and lateral mill expansion, which agrees with our results. Also, the GFIS of the HIM tightened the Gaussian beam, strengthening the central beam and weakening the tail. Thus, the fabrication result by HIM is more consistent and stable than Ga FIB. For larger grain samples like Figure 14(g, h), the nanoapertures in the annealed sample have a straighter cusp than the unannealed sample. The brighter outline in Figure 14 (c, d) also suggests a sharper edge of the nanoholes. In Figure 14 (a,b,e and f) are imaged with a scanning electron microscope at an angle. Although the eccentric point is calibrated by the instrument, the contrast of the image is still not optimized. This can also be the result of the implantation of gallium ion.

Moreover, the sidewall of the double nanohole is also affected by the grain size in depth. In Figure 11 (b and c), the grains at the buried side are usually slightly smaller than the ones on the exposure ones because of lower thermal dynamics and substrate lattice.

Spectrum measurement

To calibrate the fabricated double nanohole, I use a linear-polarized tunable telecom laser focused onto the nanoaperture sample with an intensity of 0.2 $mW/\mu m^2$. A half-wave plate is placed before the objective to control the polarization of the beam perpendicular to the long axis of the double nanohole in order to get the maximum transmission of the nanoaperture. As shown in Figure 7(c), the experiment results line up well with our numerical results on resonance shape

and position. Although the experimental data is slightly red shifted from the simulation, the corner smoothing of the gap-circle corner explains this result. The grain size of the gold layer may also have impact on the spectrum and fabrication[100].

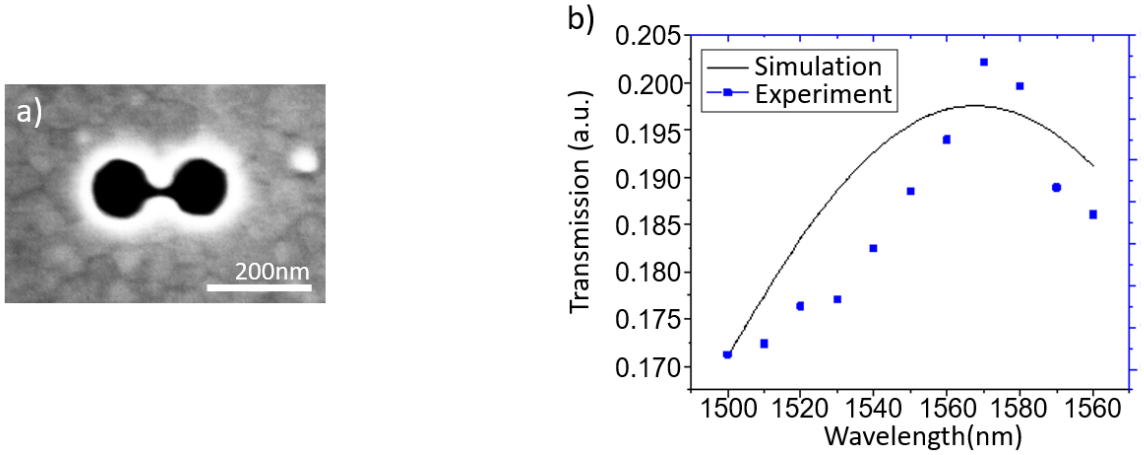

Figure 22: spectrum measurement of a DNH: a) SEM image of the DNH; b)the according simulation and experimental data of the DNH.

CHAPTER FIVE:
TRAPPING EXPERIMENT

After Bethe's theory in extraordinary optical transmission of subwavelength metallic nanoaperture, increasing research and application of the property has been explored. The zero-mode waveguide using the whispering mode in the thick film has been applied to DNA sequencing detection. However, the metallic film in this method is too thick to have a propagate mode in far field. Different from Bethe's perfect electric conductor model, Ebbesen elaborate the theory with a finite permittivity that enables the photon penetration in a real metal. The different geometries of the nanoapertures lift the cut-off wavelength to longer wavelength. Also, the wavelength of the cavity is geometry invariant, which the different geometry might have the same transparency window but different bandwidth.

The metallic nanoaperture have several benefits during interaction with dipoles: 1) The Heat conductivity of the gold protects the particles from photon-induced heat. 2) the nanozied volume surpass the background noise. 3) The small size also enhances the local electricmagnetic field and also boosts the coupling with the close-by particles. The cavity is extremely sensitive to the dielectric environment, even the particles are not on resonance. 4) The response time of the cavity is as fast as terahertz.

In this chapter, the demonstration shows the coupling of the nanoaperture and the particles with a small non-destructive power.

Setup

To separate the setup from external mechanical vibration, the trapping setup sits on a vibration isolation stage (Minus K Technology) inside a noise-insulated box. As shown in Figure 1 a), a narrow-bandwidth 1064nm laser (NKT Photonics Koheras AdjustiK) launches the beam through a 1064nm polarization-maintained optical fiber. A triplet collimator (Thorlabs TC06FC-1064) matches the beam to 1.33mm for the back-aperture size of the excitation objectives (Olympus MIR PLAN 100X, NA0.95, dry). A neutral density filter (Thorlabs NENIR02A) lowers the incident intensity to 1~4mW before a 100X excitation objective. A zero-mode halfwave plate rotates the polarization of the excitation beam perpendicular to the long axis of the double nanohole as shown in Figure 1c). The sample is placed on a nano-driver and a micro-driver from Mad Lab City, moving horizontally in an XY plane. The excitation objective is attached to the z-axis piezo driver. #2 coverslips are used during the fabrication of the metallic nanoaperture chips. The water-based solution layer is sandwiched in between a 1mm glass and the chip with the imaging spacers by Grace Bio-Labs as shown in Figure 1b). A 20X condenser (Olympus LMPlan IR) is used for signal collection and 625nm LED illumination. Note that in the following experiments, the excitation beam is lauched from the #2 glass slide and gold film to water-based solution (substrate incidence). This configuration is used to protect the nanoparticle from the excitation power. As shown in Figure 1d), the transmission of the water incident is about half of the substrate incident but the resonance wavelength remains the same. A single-pixel high-speed InGaAs Avalanche photodiode records the transmission signal over time. LabJack U60-Pro digitizes the signals with a 50~100Hz sampling rate. To find the nanoaperture, alignment markers are fabricated on the gold film. A CMOS camera is used to find the position of the alignment markers under LED

illumination. Note those makers, far away from nanoapertures (80~90 microns in diameter), do not affect the trapping process compared to 1um beam size. LED illumination is turned off during the formal experiments. All the wires and optical fibers are carefully wrapped and taped down to keep experiment consistency. Lenses are coated with a 1064nm antireflection (AR) coating if not specified.

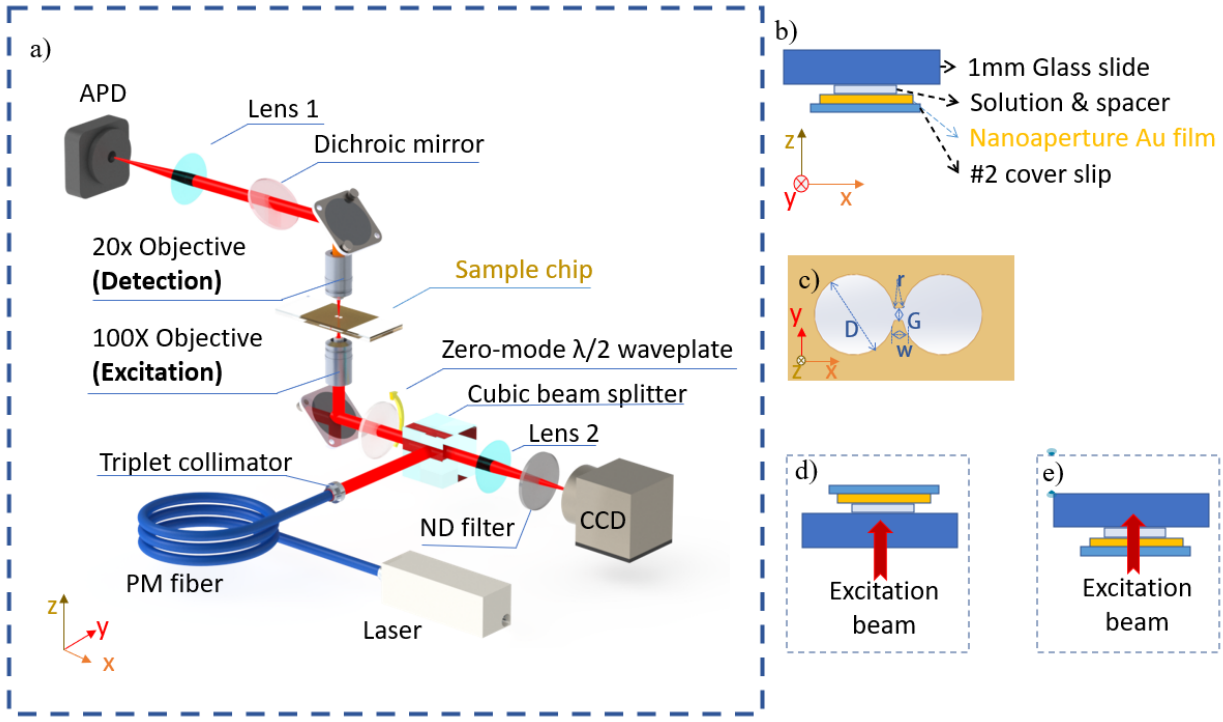

Figure 23: Setup of the trapping experiment. a) schematics of the trapping setup where APD is short for avalanche photodiode, ND filter is short for neutral density filter and PM fiber is polarization-maintained fiber; b) sample configuration of substrate excitation: the incident beam propagates along z-direction through a #2 coverslip, a gold film with DNH and then the solution and 1mm glass slide; c) nearfield simulation of the DNH; sample configuration that d) beam incident from the water solution than gold film and e) beam incident from gold substrate side then solution.

The quantum dot solution is 0.01~0.2% w/v from 1mg/1mL water-based CdSe/ZnS quantum dot solution (NN Labs, CZW-O). The core diameter is 6.9nm, coated with carboxylic acid. The emission band is 590nm which is not resonant to the 1064nm excitation beam.

The 1mm glass slide is treated with 1M KOH solution for 20min to minimize non-specific binding and maximize the lifetime of the sample. Usually, the sample lasts for 1~2 days in its original status where the particles are freely floating in the solution without adsorbed in the vicinity of the observation area (gap area).

Dynamic light scattering

Dynamic light scattering is a useful and mature technology to study the hydrodynamic diameter of particles suspended in the solution. The light is split into a reference beam and a sample beam. The sample beam encounters the particles and scatters in all directions. The two beams have a phase shift due to the scattering. So the field amplitude of the two beams is either constructive or destructive, of which visibility of the interference can be illustrated by the first-order correlation function:

$$\langle I \rangle = 2I_0[1 + |g_1(\tau)|\, cos\big(\, \omega_0 t + \varphi(\tau)\big) \tag{26}$$

$$g_1(\tau) = \frac{\langle E(t)E(t+\tau)\rangle}{\langle E(t)E(t)\rangle} = |g_1(\tau)|e^{i(\omega_0 t+\varphi(\tau)} = \beta e^{i(\omega_0 t+\varphi(\tau))} \tag{27}$$

$g_1(\tau)$ or β is the line shape of the beam. β =1 when monochromatic light. $\beta = e^{-(\frac{\tau}{\tau_c})^2}$ when the source is a broadband light and τ_c stands for coherence time. According to Siegert relation[101], the second-order and first-order correlation is coupled:

$$g_2(\tau) = B + \beta|g_1(\tau)|^2 \tag{28}$$

$$g_2(\tau) = \frac{\langle I(t)I(t+\tau)\rangle}{\langle I(t)I(t)\rangle} \tag{29}$$

As shown in the equation, $g_2(\tau)$ is the intensity correlation of the two beams. In this case, the experiment is simplified by using intensity detectors instead of field interference measurement[102]. B is the baseline of the experiment determined by the system calibration. The temporal correlation result of the two beams reflect the diffusion behavior of the particle of interest[103].

In the solution, the particle is pushed by the solvent particle and moves randomly and continuously in the solvent (Brownian motion). When interacting with the beam, the particle scatters the light and creates a phase delay of the scattered beam. The movement of the particle can be in or out of the direction of the beam[104]. Namely, the delay forms a Doppler broadening of the beam. The diffusion coefficient D_τ can be obtained from the photon correlation of the DLS. The term in equation 3.5.2.3 is

$$g_2(\tau) = B + \beta^2 e^{-2D_\tau q^2 \tau} \quad (30)$$

$$q = \frac{4\pi n}{\lambda} \sin\left(\frac{\theta}{2}\right) \quad (31)$$

q is a Bragg wavevector related to the solvent refractive index n. The detection angle θ is usually 90° for small particles to diminish the rotational diffusion effect in the autocorrelation. This back-scattering technique also allows the detection of a high-concentration sample with less multiple-scattering effect.

The diffusion coefficient D_τ is essential to measure the hydrodynamic radius R_h of the particle according to the Einstein equation:

$$D_\tau = \frac{k_B T}{6\pi\eta R_h} \quad (32)$$

k_B is Boltzmann coefficient. T is the absolute temperature. η is the viscosity of the solvent. Also, the second application of the diffusion coefficient D_τ is to determine the shape coefficient of the particles.

$$f = \frac{RT}{N_A D_\tau} \quad (33)$$

R is gas constant and N_A is Avogadro's number. According to Rayleigh's theory, the mass of the particle is proportional to its volume. the larger sizes of the particles result in a different D_τ and can be converted to a volume-weighted distribution. The DLS are widely used to detect aggregation of proteins (~100kDa), protein-small molecules interactions, conformation dynamics.

However, DLS also has some limitations in temperature sensitivity, difficulty to different particle sizes in similar sizes. It also requires transparent, non-radiative samples at a certain concentration. The high concentration sample might trigger a multi-scattering effect and leads to a lower resolution.

Hydrodynamic diameter

The soft matter is built up, ions or molecules between the surface of the charged particle and the water. As dissolved in water, the adsorbed double layer (electric double layer, EDL) is developed on the surface of the particle[105]. As shown in Figure 24, due to the electrostatic field of the charged NPs, a diffuse layer consisting of both the same and opposite charged ions/molecules grow beyond the Stern layer which along with the Stern layer forms the EDL. The inner layer with all opposite-charged ions is the Stern layer. Beyond the Stern layer, the electrostatic potential of the dispersant decreases exponentially as the distance from the particle surface increases. The zeta potential reflects the potential difference between the electric double

layer and the layer of dispersant around them at the slipping plane. Experimentally, the dispersant layer is only several nanometers from the Stern layer. The structure of this outer layer is dynamic and varies by a variety of factors e.g., pH, ionic strength, concentration, etc. An applied electric field can guide the charged particle towards the opposite electrode. This EDL affects the friction or viscosity of the liquid around the particle and changes the electrophoretic mobility of the particle. In DLS, the diameter of the particle is determined from the cumulants analysis and the scattered beam intensity. Therefore, the mobility change affects the measured size (hydrodynamic diameter). The hydrodynamic radius is a radius of the hypothetical hard-sphere, which also provides the information on the solvent effect.

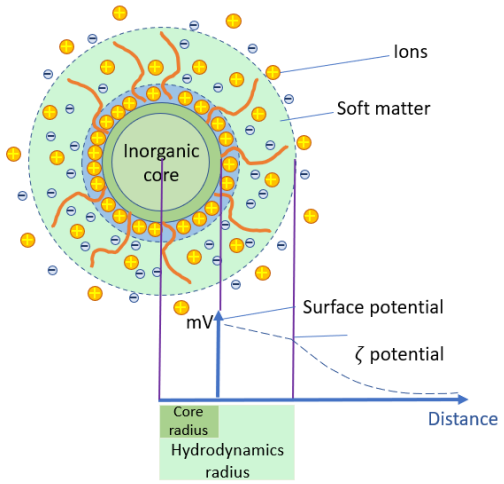

Figure 24: hydrodynamics of the negatively charged nanoparticles with different ligands. Sketch of the hydrodynamics around the inorganic core is made of soft matter and ions, where the hydrodynamic diameter is defined at the plan of zeta potential.

Quantum dots with ligands

To avoid aggregation in water solution, some monodisperse particles (quantum dots, gold nanoparticles etc.) are engineered with ligands on the surface[106]. The Van de Waals force and the electrostatic repelling force due to the zeta potential between the particles are balanced by the

ligand engineering process. The ligands also help to improve the stability of QD in biological buffers (ion and pH), maintain high quantum yield, protect the QD from quenching and have functional groups to conjugate with biomolecules. As we measured, the commercial CdSe/ZnS quantum dots have a hydrodynamic diameter of 21nm~24nm, which is much larger than the core size of the quantum dots 6.9nm. The Mn-doped ZnS QD shows different hydrodynamic diameters under different concentrations while the core size is 3nm as shown in Figure 25b) and c). The hydrodynamic size is dropped with an increasing concentration of the QD.

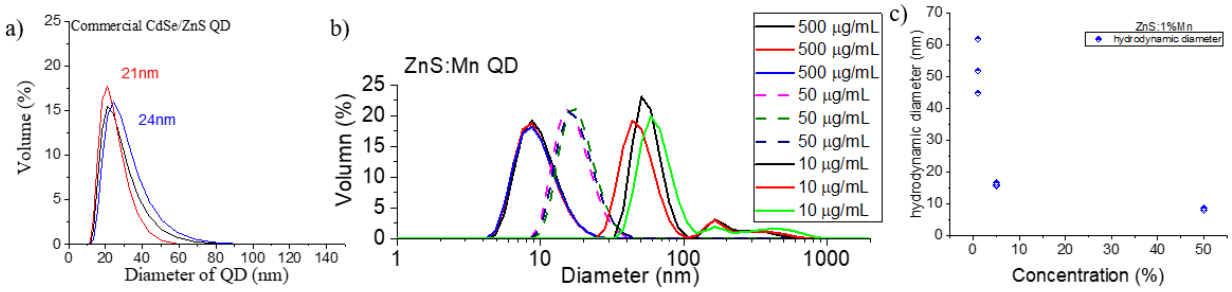

Figure 25: the dynamic light scattering measurement of b) commercial quantum dots with a core size 6.9nm and d) and e) the hydrodynamics diameter of Mn-doped ZnS quantum dots in different concentrations. a) and b) are of semilogical scale.

The hydrodynamic size on the other hand means the interaction volume of the quantum dots with the free space beam. The size of the monodispersed particles should be smaller than the gap size of the nanoparticle in the following trapping experiment.

Trap sub 10nm gold nanoparticles

In the experiments, we find the concentration does not affect much in terms of the trapping signal[107]. However, the solution concentration changes the waiting time for trapping events. In most experiments of the quantum dots and gold sphere, the concentration is above 109 particles

per milliliter or 0.2~1% w/v concentration from the 1mg/mL original sample solution. The nanoaperture is first tested with gold nanoparticles for its high polarizability. To avoid particles sticking in the gap, the size of the nanogold sphere (AuNP) is below 10nm and the gap size is 15~27nm. The size of the AuNP ranges from 5~10nm in a dynamic light scattering measurement as shown in Figure 26 c).

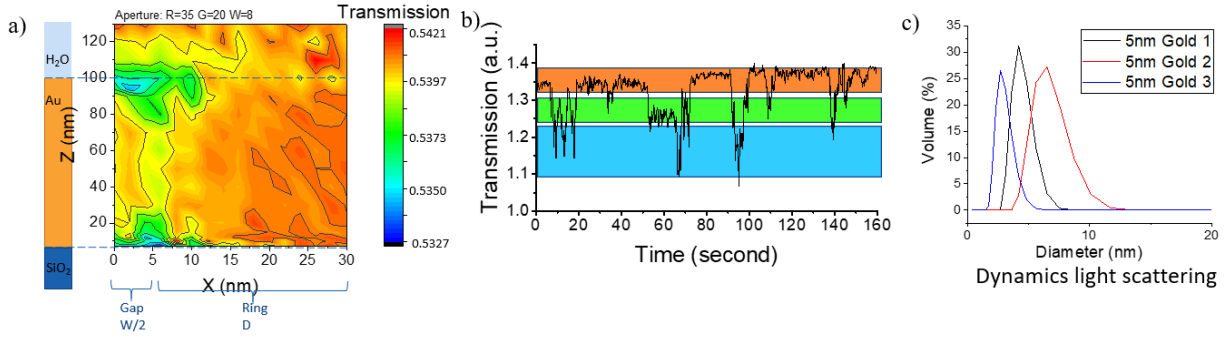

Figure 26:trapping event of 5nm gold particles: a) simulation of the position of the gold particle along the z and x-axis of the gap area, b) time trace of DNH transmission with the 5nm gold particle trapped; d) DLS result of 5nm gold particles.

The AuNP is freely diffused in the solution reservoir above the gold film. The beam wavelength is 1064nm and the resonance of the nanoaperture is around 1100nm. This is called a red-shifted regime where the wavelength of the DNH is larger than the trapping beam wavelength. Based on the simulation map of the particle position relevant to the DNH in Figure 26a), the transmission amplitude is changed when the particle diffuses close to the gap area. The X-direction is along the long axis of the DNH, where the 20nm gap area is from x = 0nm to x=4nm. The Z-direction represents the direction of beam propagation. The film thickness is from z = 0nm to z = 100nm. The negative Z is the cover glass and above z = 100nm is the water reservoir. The beam is propagated from negative z to positive z. Namely, from the cover glass to film and then the water. Due to the Brownian motion, the variance change of the trapping signal represents the

Brownian motion of the particle. The particle moving close to the corner of the gap at the water-metal interface induces a deep drop in the transmission of a red-shifted nanoaperture. Also, the transmission changes significantly when at the glass-metal interface. At the corners, the near field coupling is very strong, and the k-space is large while the transmission is higher. This results in a stronger transmission shift. In the ring area, however, the particle does not induce a strong amplitude change. Therefore, the observation area of the DNH is only at the 20nm gap area but not the rings. Meanwhile, the transmission signal is dropped several times in the 160s trace, suggesting the NAOT is not an invasive method and observe the particle freely diffused in the solvent. The observation period is around the 20s to 30s.

Trap 6.9nm quantum dots

To explore the trapping ability, the second step is to trap a different material. I choose off-resonant quantum dots as an experiment object for their comparable size to the AuNP. I also test different nanoapertures of different resonances relative to the beam wavelength. As mentioned before, the aperture resonance is larger than beam wavelength is called the red-shifted regime. Meanwhile, the aperture resonance is around 950~990nm is called the blue-shifted regime. These two regimes have opposite direction of the amplitude shift according to the theory as discussed in Chapter 2. To exam the DNH, the experiments are designed as followed.

Three regimes of traps

Figure 27 shows the time evolution of the transmitted optical power through a double-nanohole with 20 ± 2 nm tip separation. For different regimes, the nanoapertures resonate at 950nm for the blue-shifted regime, 1040nm for the coincidence regime and 1100nm for the red-shifted

regime. We used a 500Hz sampling rate with a Savitzky-Golay algorithm applied for noise reduction. The signal has a 0.2~0.5% jump in the blue and red-shifted regimes. In the blue-shifted regime, the transmission is increased. In the red-shifted regime, the particle induces a dip in amplitude. All three regimes show significant standard deviation changes due to the Brownian motion of the trapped nanoparticles. The position and conformation of the particle slightly affect the resonance spectrum and transmission amplitude as discussed in Chapter 3. The transition from an empty to an occupied trap is clear and faster than 2 seconds in general. The trapping signal lasts over 40 seconds, even up to minutes. Note that the regime of the trapping is based on the sign of the amplitude change instead of the detuning of the wavelength. the coincidence regime happens at a 1040nm DNH for the CdSe QD while the red- and blue- shifted regimes are the DNH resonant above and below 1040nm accordingly. Due to the different polarizability of the particle (material, shape, size and etc.), the spectrum shift is different.

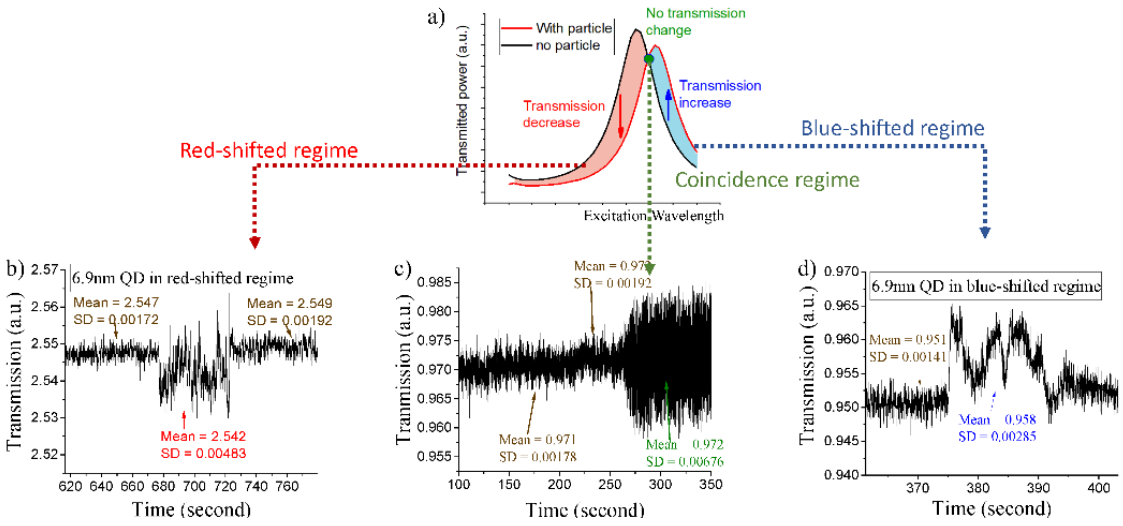

Figure 27: CdSe/ZnS quantum dots trapped in the nanoapertures of (b) red-shifted regime, (c) coincidence regime, (d) blue-shifted regime.

Figure 27d) shows the trapping of a single 6.9 nm quantum dot. 0.7% transmission decreases when the particle is trapped in the nanoaperture in the blue-shifted regime. Although the trapping signal looks periodically fluctuating, the autocorrelation result shows the randomness of the signal. This result is reasonable for the particle, randomly diffusing in the solvent due to Brownian motion. In other words, the NAOT system might have few impacts on the particle and does not intrude on the particle behavior in solution. As shown in Figure 28, the standard deviation (SD) of the trapping signal reflects the Brownian motion of the particle. For the same QD size, the standard deviation increases when the nanoaperture rensonance close to coincidence regime. on the contraray, the SD is smaller within an off-resonant particle. The nanoaperture is more sensitive to the position change in the blue-shifted regime close to the coincidence regime. The nanoaperture should be designed at 1000 ± 15nm for better sensitivity of the blue-shifted regime.

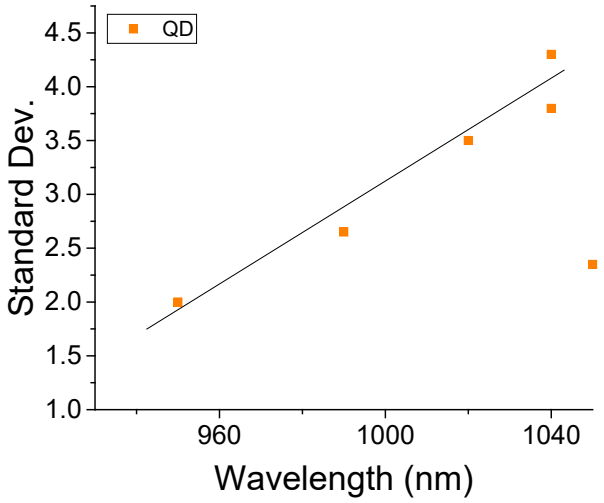

Figure 28:The standard deviation of the trapping signal of the quantum dots vs the resonance wavelength of the DNH. The coincidence regime happens to the 1040nm DNH.

The amplitude shift is shown in Figure 29. The experimental data follows the simulation curves of a nanoaperture with a 12nm CdSe sphere (black solide line) and a 8nm CdSe sphere (black dot line). The measurement shows the QD size falls into 8~10nm in diameter. Compared with the DLS result, the measured diameter is close to the core size of the QD. Therefore, NAOT can easily derive the particle size by measuring the amplitude shift. NAOT does not need the complex calibration and calculation of the diffusion coefficient. The measured diameter is a little bit larger than the core size due to the ligand size. Those ions around the particle might be in effect to the interaction volume of the particle-nanoaperture system.

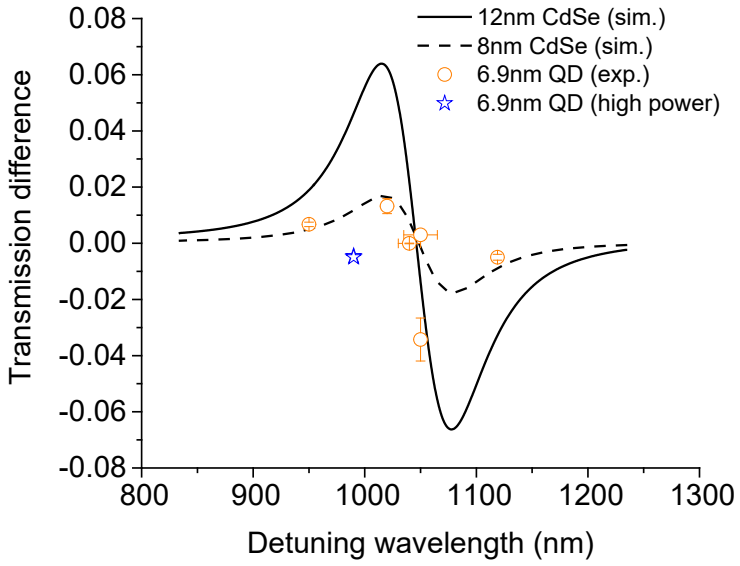

Figure 29: experiment data of the quantum dot trapped in different nanoapertures with different resonance and simulation result of the amplitude change due to the CdSe induced spectrum change. The black lines (both solid and dot) are the simulation data. The orange circles and the blue dots are the experimental data with low and higher power.

Comparison of gold and quantum dots trapping signals

In our experiment, the 5nm gold sphere is calculated as 3.4×10^5 Å^3. The polarizability of the 6.9nm colloidal CdSe/ZnS quantum dot is calculated as 8.0×10^4 Å^3, which agrees with Wang *et al*'s result ~10^4 Å^3[36].

The spectrum shift of the cavity is due to the polarizability of the particle, where the local near field of the nanoaperture is coupled with the electrons (of the metal sphere) or exciton pair (of semiconductor) as shown in Figure 28a~c). The transmission shift depends on the material of the particles. Figure 28d) shows the simulation of the transmission spectrum of the same size gold nanoparticle (red) and QD (pink) inside a DNH. The gold nanoparticles red-shift the spectrum over twice a time than QD. To validate the simulation, the solution of 5nm gold nanoparticle and QD is measured. Note these two experiments are done with different DNH chips but the same DNH geometry. The different background signal is due to the APD gain and software scaling. The result shows, the gold particle triggers over a 2% amplitude shift while the QD has less than 0.5% shift. This signal difference of one order of magnitude the potential of the NAOT to identify different material due to the difference of the particle polarizability.

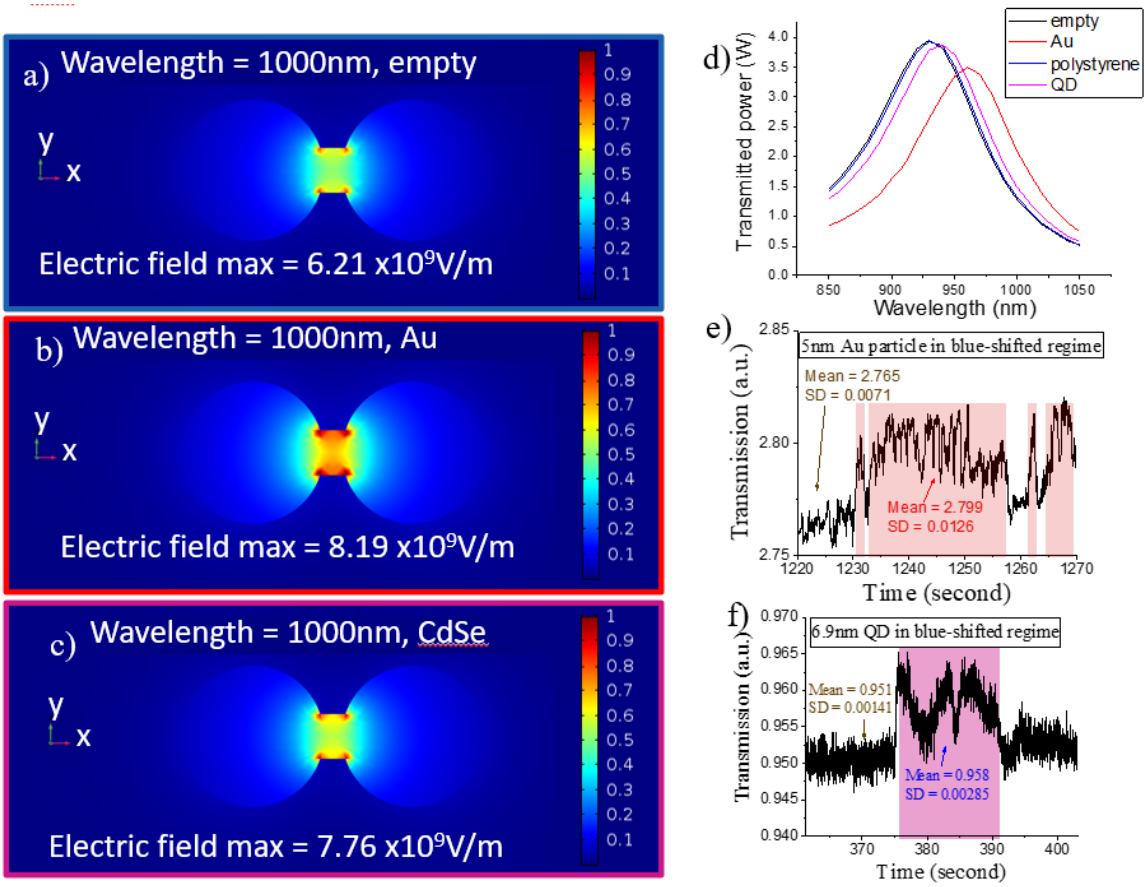

Figure 30: comparison of the trapping signals of the gold sphere and quantum dots: near field simulation of a) empty cavity, b) 16nm gold sphere and c) 16nm CdSe sphere; transmission spectrum of the empty cavity and occupied cavity with 16nm polystyrene, AuNP and QD; time trace of e) AuNP and f) QD.

Exciton-polariton from the QD trapping

What happens to the transmission of the nanoaperture with a relative stronger field in the nanoaperture? Two methods can be used to achieve the condition: 1) to increase the incident power and the ad-hoc enhancement in the gap area will increase accordingly. 2) to increase the size of the particle and the field between the particle surface and gap is significantly increased. Under a weak field, the optical wavelength is far from the absorption of the QD. The electrons of the QD is in the ground state. The CdSe QD induces a positive polarizability in the dielectric environment[108]. Under a relative stronger field, the optical absorption of the QD is not linear

and the exciton is generated. The dipole interaction from the QD should not be ignore[109]. The strength of the absorption is depended on the polarization of the field in the aperture. The polarization is characterized by its amplitude and phase. The incoherent field has no phase information. The phase determines the optical absorption spectrum and therefore the strength of the exciton resonances. The amplitude determines the optically induced refractive index changes. The free carrier has a lifetime before its recombination, introducing a phase difference to the external field. The excited exciton-polariton requires negative permittivity which induces a negative polarizability to the nanoaperture.

In the experiments, we also observe the larger local field amplitude in two different nanoapertures with similar geometry parameters (gap size 15nm, gap length 17nm and ring diameter 60nm). The power is above >3.9mW at the sample. The nanoaperture is resonant at 990nm, the QD triggers an amplitude dip instead of a surge as shown in Figure 29 c). Two explanations can be applied here: 1) the phase retardation of the QD leads to the asymmetric profile of the transmission spectrum. Compared with the damping rate of QD (ns), the DNH has a much faster damping rate (ps). Thus, under the drive of the external field, QD absorbs the energy with a phase shift. The opposite phases between the QD and the DNH cavity interfere with each other, lead to Fano-shape transmission spectra, and have a decrease of the transmission upon trapping. 2) TM wave at the interface excites surface plasmonic polaritons along the metal-dielectric boundary. The evanescent field extends perpendicular to the interface. Due to the high dispersion [57], these polariton modes on the QD are much smaller than the wavelength but extremely high local density of optical states, leading to strong light-matter interaction. For the polariton at semiconductor and dielectric interface, the free carriers, other than electrons, provides the

oscillation with the photons. These are called exciton-polaritons. Their similar behavior to plasmonic-polariton in metal suggests a negative permittivity of the free carriers and following a strong absorption of a photon, which agrees with other literature[59].

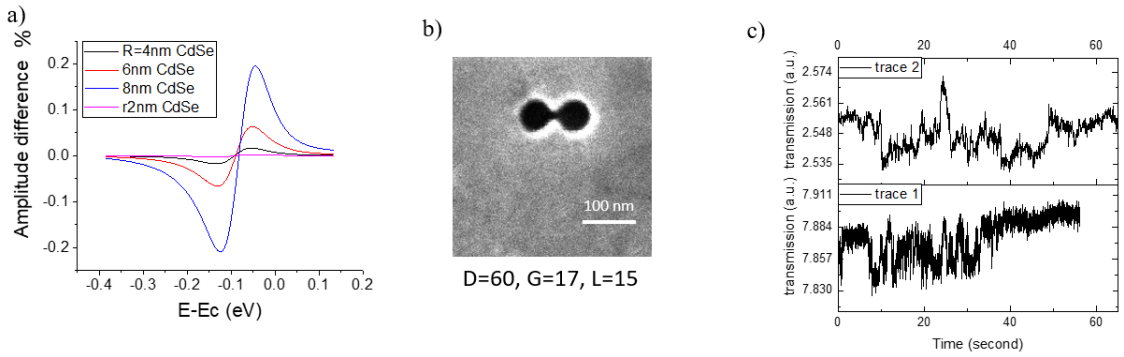

Figure 31: the experimental result of negative polarizability: a) transmission simulation of nanoaperture with different incident energies shows the Fano-shape of the coupling; b) helium ion microscope image of the double nanohole with gap size = 60nm, Gap distance = 15nm and diameter = 60nm where the scale bar is 100nm; c) two transmission traces from two nanoapertures shows repeatable dips in amplitude upon trapping. Trace 1 has 0.01s time resolution while trace 2 has 0.5s.

In weak coupling, the quantum dot is simply a dipole in a plasmonic cavity, the same as gold. It follows the same phenomena in different DNHs. However, when the incident power increases and the gap size is similar to the particle, the near field enhancement in the gap area surges. The strong field affects the quantum dot and triggers other absorption. In this case, the dipole approximation does not work. Instead, the quantum dot should be regarded as an oscillator. The absorption of the quantum dots might from exciton generation or two-photon absorption. Thus, the quantum dots behave differently from the weak coupling regime, namely, a dip of amplitude upon trapping.

In this experiment, the result suggests that the local EM field increases the transmission. however, the strong local field might also interfere with particle absorption. The hydrodynamic

diameter serves as an interaction volume of the quantum dot suggests the size of the gap should be larger than (4nm for 20nm gap) the QD.

CHAPTER SIX: CONCLUSION

In this thesis, we discussed the theory, design, fabrication and experimental results of the NAOT. The plasmonic effect excites the local near field and increases the transmission through a subwavelength nanoaperture. The geometry design of the nanoaperture shows that the transmission spectrum is not limited to a certain geometry. The different structures can have similar transmission central wavelengths, but the bandwidths can be affected. The DNH has a better performance in corner-smoothing effect in the transmission spectrum than the bowtie structure. Therefore, the DNH is much easier and more robust for fabrication.

I also promote the fabrication resolution by using a three-step sample preparation procedure: evaporation, low-temperature annealing and template stripping. The grain boundary increases the intrinsic strain in the material and the multi-scattering of the electrons. This procedure significantly increases the grain sizes to 1micron in diameter and decreases the surface roughness to 0.2nm. The sample preparation improves the optical property of the film and leaves a better playground for the following lithography of the double nanohole. The total length of the double nanohole is about 200nm, which can be fit in a single grain. With the help of the helium ion beam lithography, the fabricated geometry has good consistency with the design. The sidewall of the nanoaperture is clean and smooth.

By using the sensitivity of the plasmon-polariton on the dielectric-metal interface, the transmission spectrum of the nanoaperture is applied to observe the presence of the nanoparticles. Detuning the wavelength of the excitation beam and the nanoaperture results in the opposite transmission amplitude shift, suggesting the transmission spectrum shift to a longer wavelength. The amplitude of the transmission change and the standard deviation can both be used to measure

the size of the particle with *a priori* of the permittivity of the material without complex calculation of diffusion coefficient. The comparison between the quantum dots and gold particles finds the polarizability can be reflected in the transmission evolution. The transmission of the gold is one order larger than the quantum dot. In the last experiment, we find the volume ratio of the particle and gap size is also important to the trap. When the two oscillators are close in size, the coupling becomes stronger. The Purcell effect would increase the amplitude of the spontaneous emission of the cavity but the phase interference between the two oscillators might cancel each other and result in a decrease in amplitude. Also, the local intensity should be limited for trapping purposes. The nonlinear effect and heat are easier to disturb the NAOT efficiency with a higher local field. With the test of different material of the particle, this thesis leaves fundamental guidance of the NAOT for further application such as protein, DNA and other biomolecules. It leaves a solid foundation for NAOT to study the conformation, shape of the biomolecules. NAOT also take advangtage of the fast response of the cavity (picosecond). The measurement limitation is attributed to the detector speed. With a GHz single pixel APD, this method can be applied to study fast disassociation process and protein-small molecule interaction.

REFERENCES

1. Roberts, T.C., R. Langer, and M.J.A. Wood, *Advances in oligonucleotide drug delivery.* Nature Reviews Drug Discovery, 2020. **19**(10): p. 673-694.
2. Zeidell, A.M., et al., *Organic Semiconductors Derived from Dinaphtho-Fused s-Indacenes: How Molecular Structure and Film Morphology Influence Thin-Film Transistor Performance.* Chemistry of Materials, 2019. **31**(17): p. 6962-6970.
3. Simpson, D.A., et al., *Non-Neurotoxic Nanodiamond Probes for Intraneuronal Temperature Mapping.* ACS Nano, 2017. **11**(12): p. 12077-12086.
4. Kim, M.E., et al., *Trapping single atoms on a nanophotonic circuit with configurable tweezer lattices.* Nature Communications, 2019. **10**(1).
5. Liu, S., et al., *Efficiently Passivated PbSe Quantum Dot Solids for Infrared Photovoltaics.* ACS Nano, 2021.
6. Gaita-Ariño, A., et al., *Molecular spins for quantum computation.* Nature Chemistry, 2019. **11**(4): p. 301-309.
7. Guidelli, E.J., A.P. Ramos, and O. Baffa, *Enhancing and quenching luminescence with gold nanoparticle films: the influence of substrate on the luminescent properties.* Nanotechnology, 2015. **27**(1): p. 015503.
8. Guzman-Sepulveda, J.R., et al., *Tubulin Polarizability in Aqueous Suspensions.* ACS Omega, 2019. **4**(5): p. 9144-9149.
9. Miller, H., et al., *Single-molecule techniques in biophysics: a review of the progress in methods and applications.* Reports on Progress in Physics, 2018. **81**(2): p. 024601.
10. Mickolajczyk, K.J., et al., *Kinetics of nucleotide-dependent structural transitions in the kinesin-1 hydrolysis cycle.* Proceedings of the National Academy of Sciences, 2015. **112**(52): p. E7186-E7193.
11. Michalet, X., et al., *Detectors for single-molecule fluorescence imaging and spectroscopy.* Journal of Modern Optics, 2007. **54**(2-3): p. 239-281.
12. Ortega-Arroyo, J. and P. Kukura, *Interferometric scattering microscopy (iSCAT): new frontiers in ultrafast and ultrasensitive optical microscopy.* Physical Chemistry Chemical Physics, 2012. **14**(45): p. 15625.
13. Shen, H., et al., *Single Particle Tracking: From Theory to Biophysical Applications.* Chemical Reviews, 2017. **117**(11): p. 7331-7376.
14. Ortega Arroyo, J., D. Cole, and P. Kukura, *Interferometric scattering microscopy and its combination with single-molecule fluorescence imaging.* Nature Protocols, 2016. **11**(4): p. 617-633.
15. Strack, R., *Weighing single proteins with light.* Nature Methods, 2018. **15**(7): p. 477-477.
16. Zhao, Y., et al., *Nanoscopic control and quantification of enantioselective optical forces.* Nature Nanotechnology, 2017. **12**: p. 1055.
17. Caldwell, L. and M.R. Tarbutt, *Enhancing Dipolar Interactions between Molecules Using State-Dependent Optical Tweezer Traps.* Physical Review Letters, 2020. **125**(24).
18. Jones, S., et al., *Ultrafast Modulation of Thermoplasmonic Nanobubbles in Water.* Nano Letters, 2019. **19**(11): p. 8294-8302.
19. Karpinski, P., et al., *Optical Rotation and Thermometry of Laser Tweezed Silicon Nanorods.* Nano Letters, 2020. **20**(9): p. 6494-6501.

20. Restrepo-Perez, L., et al., *SDS-assisted protein transport through solid-state nanopores.* Nanoscale, 2017. **9**(32): p. 11685-11693.
21. Monod, J., J.-P. Changeux, and F. Jacob, *Allosteric proteins and cellular control systems.* Journal of Molecular Biology, 1963. **6**(4): p. 306-329.
22. Sato, T., J. Ohnuki, and M. Takano, *Dielectric Allostery of Protein: Response of Myosin to ATP Binding.* The Journal of Physical Chemistry B, 2016. **120**(51): p. 13047-13055.
23. Tong, M., et al., *Survey of solution dynamics in Src kinase reveals allosteric cross talk between the ligand binding and regulatory sites.* Nature Communications, 2017. **8**(1): p. 2160.
24. Yoo, D., et al., *Low-Power Optical Trapping of Nanoparticles and Proteins with Resonant Coaxial Nanoaperture using 10 nm gap.* Nano Letters, 2018.
25. Favre-Bulle, I.A., et al., *Optical trapping in vivo: theory, practice, and applications.* Nanophotonics, 2019. **8**(6): p. 1023-1040.
26. Ashkin, A., *Acceleration and Trapping of Particles by Radiation Pressure.* Physical Review Letters, 1970. **24**(4): p. 156-159.
27. Ashkin, A. and J. Dziedzic, *Optical trapping and manipulation of viruses and bacteria.* Science, 1987. **235**(4795): p. 1517-1520.
28. Berns, M.W., et al., *Use of a laser-induced optical force trap to study chromosome movement on the mitotic spindle.* Proceedings of the National Academy of Sciences, 1989. **86**(12): p. 4539-4543.
29. Zhong, M.-C., et al., *Trapping red blood cells in living animals using optical tweezers.* Nature Communications, 2013. **4**(1).
30. Friese, M.E.J., et al., *Optical angular-momentum transfer to trapped absorbing particles.* Physical Review A, 1996. **54**(2): p. 1593-1596.
31. Harris, G.I., et al., *Laser cooling and control of excitations in superfluid helium.* Nature Physics, 2016. **12**(8): p. 788-793.
32. Ashkin, A., et al., *Observation of a single-beam gradient force optical trap for dielectric particles.* Optics Letters, 1986. **11**(5): p. 288.
33. Dao, M., C.T. Lim, and S. Suresh, *Mechanics of the human red blood cell deformed by optical tweezers.* Journal of the Mechanics and Physics of Solids, 2003. **51**(11-12): p. 2259-2280.
34. Grozema, F.C., et al., *Excited state polarizabilities of conjugated molecules calculated using time dependent density functional theory.* The Journal of Chemical Physics, 2001. **115**(21): p. 10014-10021.
35. Generalov, K.V., et al., *Method for Measuring the Polarizability of Cells in an Inhomogeneous Alternating Electric Field.* Measurement Techniques, 2017. **60**(1): p. 82-86.
36. Wang, F., et al., *Exciton polarizability in semiconductor nanocrystals.* Nature Materials, 2006. **5**(11): p. 861-864.
37. Rechberger, W., et al., *Optical properties of two interacting gold nanoparticles.* Optics Communications, 2003. **220**(1-3): p. 137-141.
38. Hugall, J.T., A. Singh, and N.F. van Hulst, *Plasmonic Cavity Coupling.* ACS Photonics, 2018. **5**(1): p. 43-53.
39. Mestres, P., et al., *Unraveling the optomechanical nature of plasmonic trapping.* Light: Science & Applications, 2016. **5**(7): p. e16092-e16092.
40. Juan, M.L., et al., *Self-induced back-action optical trapping of dielectric nanoparticles.* Nature Physics, 2009. **5**(12): p. 915-919.

41. Neumeier, L., R. Quidant, and D.E. Chang, *Self-induced back-action optical trapping in nanophotonic systems.* New Journal of Physics, 2015. **17**(12): p. 123008.
42. Bohr, N., *I. On the constitution of atoms and molecules.* The London, Edinburgh, and Dublin Philosophical Magazine and Journal of Science, 2009. **26**(151): p. 1-25.
43. Xie, Z., et al., *Doubly Resonant Photonic Antenna for Single Infrared Quantum Dot Imaging at Telecommunication Wavelengths.* Nano Letters, 2017. **17**(4): p. 2152-2158.
44. Tvrdy, K., P.A. Frantsuzov, and P.V. Kamat, *Photoinduced electron transfer from semiconductor quantum dots to metal oxide nanoparticles.* Proceedings of the National Academy of Sciences, 2011. **108**(1): p. 29-34.
45. Bitton, O., S.N. Gupta, and G. Haran, *Quantum dot plasmonics: from weak to strong coupling.* Nanophotonics, 2019. **8**(4): p. 559-575.
46. Rafailov, E.U., M.A. Cataluna, and W. Sibbett, *Mode-locked quantum-dot lasers.* Nature Photonics, 2007. **1**(7): p. 395-401.
47. Chan, W.C., *Quantum Dot Bioconjugates for Ultrasensitive Nonisotopic Detection.* Science, 1998. **281**(5385): p. 2016-2018.
48. Warner, J.H. and R.D. Tilley, *Synthesis and Self-Assembly of Triangular and Hexagonal CdS Nanocrystals.* Advanced Materials, 2005. **17**(24): p. 2997-3001.
49. Bublitz, G.U. and S.G. Boxer, *STARK SPECTROSCOPY: Applications in Chemistry, Biology, and Materials Science.* Annual Review of Physical Chemistry, 1997. **48**(1): p. 213-242.
50. Colvin, V.L., K.L. Cunningham, and A.P. Alivisatos, *Electric field modulation studies of optical absorption in CdSe nanocrystals: Dipolar character of the excited state.* The Journal of Chemical Physics, 1994. **101**(8): p. 7122-7138.
51. Mehata, M.S., *Enhancement of Charge Transfer and Quenching of Photoluminescence of Capped CdS Quantum Dots.* Scientific Reports, 2015. **5**(1).
52. Jin, T., et al., *Competition of Dexter, Förster, and charge transfer pathways for quantum dot sensitized triplet generation.* The Journal of Chemical Physics, 2020. **152**(21): p. 214702.
53. Empedocles, S.A., *Quantum-Confined Stark Effect in Single CdSe Nanocrystallite Quantum Dots.* Science, 1997. **278**(5346): p. 2114-2117.
54. Purcell, E.M., H.C. Torrey, and R.V. Pound, *Resonance Absorption by Nuclear Magnetic Moments in a Solid.* Physical Review, 1946. **69**(1-2): p. 37-38.
55. Reithmaier, J.P., et al., *Strong coupling in a single quantum dot–semiconductor microcavity system.* Nature, 2004. **432**(7014): p. 197-200.
56. Leng, H., et al., *Strong coupling and induced transparency at room temperature with single quantum dots and gap plasmons.* Nature Communications, 2018. **9**(1).
57. Johnson, P.B. and R.W. Christy, *Optical Constants of the Noble Metals.* Physical Review B, 1972. **6**(12): p. 4370-4379.
58. Hopfield, J.J., *Theory of the Contribution of Excitons to the Complex Dielectric Constant of Crystals.* Physical Review, 1958. **112**(5): p. 1555-1567.
59. Chernikov, A., et al., *Exciton Binding Energy and Nonhydrogenic Rydberg Series in MonolayerWS2.* Physical Review Letters, 2014. **113**(7).
60. Polycarpou, A.C., *Introduction to the Finite Element Method in Electromagnetics.* Synthesis Lectures on Computational Electromagnetics, 2006. **1**(1): p. 1-126.
61. Mestres, P., et al., *Unraveling the optomechanical nature of plasmonic trapping.* Light: Science & Applications, 2016. **5**(7): p. e16092.

62. Berthelot, J., et al., *Three-dimensional manipulation with scanning near-field optical nanotweezers.* Nat Nanotechnol, 2014. **9**(4): p. 295-9.
63. Qiao, W., et al., *Optimizing bowtie structure parameters for specific incident light.* Chinese Physics B, 2010. **19**(11): p. 117304.
64. Jensen, R.A., et al., *Optical Trapping and Two-Photon Excitation of Colloidal Quantum Dots Using Bowtie Apertures.* ACS Photonics, 2016. **3**(3): p. 423-427.
65. Hou, Z., N.L. Abbott, and P. Stroeve, *Electroless Gold as a Substrate for Self-Assembled Monolayers.* Langmuir, 1998. **14**(12): p. 3287-3297.
66. Wheaton, S., R.M. Gelfand, and R. Gordon, *Probing the Raman-active acoustic vibrations of nanoparticles with extraordinary spectral resolution.* Nature Photonics, 2014. **9**: p. 68.
67. Katyal, J. and R. Soni, *Size-and shape-dependent plasmonic properties of aluminum nanoparticles for nanosensing applications.* Journal of Modern Optics, 2013. **60**(20): p. 1717-1728.
68. Johnson, P.B. and R.-W. Christy, *Optical constants of the noble metals.* Physical review B, 1972. **6**(12): p. 4370.
69. McPeak, K.M., et al., *Plasmonic films can easily be better: rules and recipes.* ACS photonics, 2015. **2**(3): p. 326-333.
70. Guo, H., et al., *Optical resonances of bowtie slot antennas and their geometry and material dependence.* Optics Express, 2008. **16**(11): p. 7756-7766.
71. Messinger, B.J., et al., *Local fields at the surface of noble-metal microspheres.* Physical Review B, 1981. **24**(2): p. 649.
72. Fleischmann, M., P.J. Hendra, and A.J. McQuillan, *Raman spectra of pyridine adsorbed at a silver electrode.* Chemical Physics Letters, 1974. **26**(2): p. 163-166.
73. McCall, S.L. and E.L. Hahn, *Self-Induced Transparency.* Physical Review, 1969. **183**(2): p. 457-485.
74. Juan, M.L., et al., *Self-induced back-action optical trapping of dielectric nanoparticles.* Nature Physics, 2009. **5**: p. 915.
75. Emmrich, D., et al., *Nanopore fabrication and characterization by helium ion microscopy.* Applied Physics Letters, 2016. **108**(16): p. 163103.
76. Scholder, O., et al., *Helium focused ion beam fabricated plasmonic antennas with sub-5 nm gaps.* Nanotechnology, 2013. **24**(39): p. 395301.
77. Manfrinato, V.R., et al., *Resolution limits of electron-beam lithography toward the atomic scale.* Nano letters, 2013. **13**(4): p. 1555-1558.
78. Oh, D.K., et al., *Top-down nanofabrication approaches toward single-digit-nanometer scale structures.* Journal of Mechanical Science and Technology, 2021.
79. Jassim, S.A.-J., A.A.R.A. Zumaila, and G.A.A. Al Waly, *Influence of substrate temperature on the structural, optical and electrical properties of CdS thin films deposited by thermal evaporation.* Results in Physics, 2013. **3**: p. 173-178.
80. Capper, P., S. Irvine, and T. Joyce, *Epitaxial Crystal Growth: Methods and Materials*, in *Springer Handbook of Electronic and Photonic Materials*, S. Kasap and P. Capper, Editors. 2017, Springer International Publishing: Cham. p. 1-1.
81. Westmacott, K.H., S. Hinderberger, and U. Dahmen, *Physical vapour deposition growth and transmission electron microscopy characterization of epitaxial thin metal films on single-crystal Si and Ge substrates.* Philosophical Magazine A, 2001. **81**(6): p. 1547-1578.
82. Yin, L., et al., *Subwavelength Focusing and Guiding of Surface Plasmons.* Nano Letters, 2005. **5**(7): p. 1399-1402.

83. Markert, C., D. Lützenkirchen-Hecht, and R. Frahm, *Structural and electrical properties of thin d.c. magnetron-sputtered gold films deposited on float glass.* Surface and Interface Analysis, 2006. **38**(4): p. 715-718.
84. Singh, A., *Film thickness and grain size diameter dependence on temperature coefficient of resistance of thin metal films.* Journal of Applied Physics, 1974. **45**(4): p. 1908-1909.
85. Seliger, R.L., et al., *High‐resolution, ion‐beam processes for microstructure fabrication.* Journal of Vacuum Science and Technology, 1979. **16**(6): p. 1610-1612.
86. Kollmann, H., et al., *Toward Plasmonics with Nanometer Precision: Nonlinear Optics of Helium-Ion Milled Gold Nanoantennas.* Nano Letters, 2014. **14**(8): p. 4778-4784.
87. Li, W.-D., W. Wu, and R. Stanley Williams, *Combined helium ion beam and nanoimprint lithography attains 4 nm half-pitch dense patterns.* Journal of Vacuum Science & Technology B, 2012. **30**(6): p. 06F304.
88. Belianinov, A., et al., *Noble gas ion beams in materials science for future applications and devices.* MRS Bulletin, 2017. **42**(9): p. 660-666.
89. Hlawacek, G. and A. Gölzhäuser, *Helium Ion Microscopy*. 2016: Springer.
90. Gierak, J., *Focused ion beam technology and ultimate applications.* Semiconductor Science and Technology, 2009. **24**(4): p. 043001.
91. Winston, D., et al., *Neon Ion Beam Lithography (NIBL).* Nano Letters, 2011. **11**(10): p. 4343-4347.
92. Winston, D., et al., *Scanning-helium-ion-beam lithography with hydrogen silsesquioxane resist.* Journal of Vacuum Science & Technology B: Microelectronics and Nanometer Structures, 2009. **27**(6): p. 2702.
93. Chen, H.S. and D. Turnbull, *Thermal Properties of Gold‐Silicon Binary Alloy near the Eutectic Composition.* Journal of Applied Physics, 1967. **38**(9): p. 3646-3650.
94. Abbott, W.M., et al., *Solid state dewetting of thin plasmonic films under focused cw-laser irradiation.* Acta Materialia, 2018. **145**: p. 210-219.
95. Zhang, C., et al., *Nanoaperture fabrication in ultra-smooth single-grain gold films with helium ion beam lithography.* Nanotechnology, 2020. **31**(46): p. 465302.
96. Mayer, J., et al., *TEM Sample Preparation and FIB-Induced Damage.* MRS Bulletin, 2011. **32**(5): p. 400-407.
97. Ward, B.W., J.A. Notte, and N.P. Economou, *Helium ion microscope: A new tool for nanoscale microscopy and metrology.* Journal of Vacuum Science & Technology B: Microelectronics and Nanometer Structures Processing, Measurement, and Phenomena, 2006. **24**(6): p. 2871-2874.
98. Wang, Y.D., et al., *Grain-orientation-dependent residual stress and the effect of annealing in cold-rolled stainless steel.* Acta Materialia, 2002. **50**(7): p. 1717-1734.
99. Allen, F.I., et al., *Gallium, neon and helium focused ion beam milling of thin films demonstrated for polymeric materials: study of implantation artifacts.* Nanoscale, 2019. **11**(3): p. 1403-1409.
100. Yakubovsky, D.I., et al., *Optical constants and structural properties of thin gold films.* Optics Express, 2017. **25**(21): p. 25574-25587.
101. Siegert, A.J.F., *On the Approach to Statistical Equilibrium.* Physical Review, 1949. **76**(11): p. 1708-1714.
102. Pecora, R., *Quasi-Elastic Light Scattering from Macromolecules.* Annual Review of Biophysics and Bioengineering, 1972. **1**(1): p. 257-276.
103. Foord, R., et al., *Determination of Diffusion Coefficients of Haemocyanin at Low Concentration by Intensity Fluctuation Spectroscopy of Scattered Laser Light.* Nature, 1970. **227**(5255): p. 242-245.

104. Harding, S.E. and K. Jumel, *Light Scattering.* Current Protocols in Protein Science, 1998. **11**(1).
105. Bhattacharjee, S., *DLS and zeta potential – What they are and what they are not?* Journal of Controlled Release, 2016. **235**: p. 337-351.
106. Zhang, Y. and A. Clapp, *Overview of Stabilizing Ligands for Biocompatible Quantum Dot Nanocrystals.* Sensors, 2011. **11**(12): p. 11036-11055.
107. Kotnala, A., et al., *Overcoming Diffusion-Limited Trapping in Nanoaperture Tweezers Using Opto-Thermal-Induced Flow.* Nano Letters, 2019. **20**(1): p. 768-779.
108. Alves-Santos, M., R.D. Felice, and G. Goldoni, *Dielectric Functions of Semiconductor Nanoparticles from the Optical Absorption Spectrum: The Case of CdSe and CdS.* The Journal of Physical Chemistry C, 2010. **114**(9): p. 3776-3780.
109. Fu, Y., L. Thylén, and H. Ågren, *A Lossless Negative Dielectric Constant from Quantum Dot Exciton Polaritons.* Nano Letters, 2008. **8**(5): p. 1551-1555.
110. Ghimire, S. and V. Biju, *Relations of exciton dynamics in quantum dots to photoluminescence, lasing, and energy harvesting.* Journal of Photochemistry and Photobiology C: Photochemistry Reviews, 2018. **34**: p. 137-151.